

Local radial basis function based gridfree scheme for unsteady incompressible viscous flows

Y.V.S.S. Sanyasiraju^{*}, G. Chandhini

Department of Mathematics, Indian Institute of Technology Madras, Chennai 600036, India

ARTICLE INFO

Article history:

Received 23 November 2007

Received in revised form 27 June 2008

Accepted 6 July 2008

Available online 17 July 2008

PACS:

47.10.ad

47.11.Bc

47.15.Rq

Keywords:

Radial basis function

Multiquadric

Fractional step

Unsteady

Incompressible

Navier–Stokes equations

ABSTRACT

A 'local' radial basic function (RBF) based gridfree scheme has been developed to solve unsteady, incompressible Navier–Stokes equations in primitive variables. The velocity–pressure decoupling is obtained by making use of a fractional step algorithm. The scheme is validated over a variety of benchmark problems and found a very good agreement with the existing results. Comparisons with the benchmark solutions show that the developed local RBF gridfree scheme is stable and produces accurate results on domains discretized even with non-uniform distribution of nodal points.

© 2008 Elsevier Inc. All rights reserved.

1. Introduction

In order to reduce the high cost of grid generation, numerous schemes have been proposed in the last two decades. Grid-free schemes are one such class of methods in which the solution is approximated on a set of nodes with no specified connectivity. Smoothed particle hydrodynamics, element free Galerkin method, reproducing kernel particle method, the partition of unity method, the hp-clouds method, finite point method, mesh less Petrov–Galerkin method and general finite difference method are the well known gridfree methods considered for fluid flow problems.

Another group of gridfree methods for partial differential equations (PDEs), based on radial basis functions (RBFs), are currently undergoing tremendous research. Over the last few decades RBFs have been very successfully investigated for reconstructing functions from multivariate scattered data. This success led Kansa [1] to initiate the use of RBF interpolation in the global collocation methods for solving partial differential equations. Following this, Fasshauer [2] proposed another collocation method based on Wu's [3] Hermite-RBF interpolation. The resulting collocation matrix obtained in Fasshauer's approach is symmetric and non-singular, while the matrix obtained in Kansa's approach is non-symmetric and also the non-singularity is not guaranteed, as shown by Hon and Schaback [4] (even though such situations are rare in practical problems). Using asymmetric collocation method, heat transfer and fluid dynamics problems have been studied by Chantasiriwan [6] and Šarler [5]. A third collocation approach has been proposed by Mai-Duy and Tran-Cong [7] and Mai-Duy et al. [8] for which

^{*} Corresponding author. Tel.: +91 44 22574621; fax: +91 44 22574602.

E-mail addresses: sryedida@iitm.ac.in (Y.V.S.S. Sanyasiraju), chandhini@iitm.ac.in (G. Chandhini).

the basis functions are taken to be anti-derivatives of the usual radial basis functions with the expectation that the resulting system is more stable due to the involvement of integrals rather than derivatives. Other significant contributions made in this direction are the works of Chen and Hon [9], Chen and Tanaka [10] and Chen et al. [11].

In all the investigations mentioned above, it is necessary to invert a highly ill-conditioned dense matrix due to the globally supported RBFs. Moreover, the amount of computation increases when these methods are applied for nonlinear or time-dependent problems. To circumvent these difficulties some alternatives have been proposed in the literature, namely, domain decomposition, preconditioning and the use of compactly supported RBFs. Recently, an RBF based ‘local’ method has been proposed by Wright and Fornberg [12]. In their method, derivatives are approximated in the same manner as in the case of traditional FD schemes. In essence, discretization of the derivatives at any particular node is obtained by RBF interpolation using a small set of nodes in the neighborhood, which forms a stencil as in FD. Wright and Fornberg tested their schemes by applying them to Poisson type of equations. Some more efforts to bring localization in RBF-based methods have been independently made by Lee et al. [13], Tolstykh and Shirobokov [14], Šarler and Vertnik [15] and Vertnik and Šarler [16]. The methods in [13,14], though used different procedure, has a similar form of [12]. A direct localization of the global collocation method has been considered in [15,16].

In the present work, the development of a gridfree scheme, based on the localizing concept proposed by Wright and Fornberg [12], to solve unsteady incompressible viscous flows and its application to some simple and complex benchmark flow problems has been presented. The governing equations of the fluid flow are taken in primitive variables due to their general nature. This form of Navier–Stokes equations requires a special procedure to compute the pressure from the continuity equation. SIMPLE-type of algorithms have originally been developed for steady incompressible Navier–Stokes equations, especially on staggered grid arrangement. However, such pressure correction algorithms are computationally very expensive for transient problems due to a nested three loop iterative procedure (an additional time iteration over two usual nested iterative processes of the steady SIMPLE procedure). Therefore, nearly all numerical methods for solving unsteady incompressible flow equations in terms of the primitive variables [17–19] use a fractional step approach. The basic idea behind these algorithms is to get some approximation for the velocity components from the momentum equations and then solving an elliptic equation to enforce the divergence free constraint, which in turn determines the pressure. The proposed algorithm also follows a similar procedure but, uses local gridfree RBF scheme to discretize its spatial derivatives.

The organization of the paper is as follows: the local interpolation problem using radial basis functions and the development of a local gridfree scheme to solve general boundary value problems is presented in Section 2. The development of the scheme to solve incompressible Navier–Stokes equations is given in Section 3. In Section 4, the developed scheme has been validated using variety of benchmark problems and compared the obtained results with the existing ones.

2. Development of the local RBF scheme

2.1. Interpolation using radial basis functions

Radial basis functions are initially known as a powerful tool for approximating multivariate functions on a scattered data. These functions can be broadly classified into infinitely smooth and piecewise smooth radial functions. The former includes a shape parameter ε , by varying which the radial function can be varied from sharp peaked one to a very flat one. Classical choices of RBFs are given in Table 1 along with their order m . The order of a radial basis function represents the minimum degree of the polynomial to be appended to the interpolant to ensure the non-singularity of the interpolation matrix.

Multiquadric (MQ), an infinitely smooth RBF, is one among the most popular radial functions. Hardy [20] was the first to derive the two-dimensional MQ scheme to approximate geographical surfaces. Franke, in his survey [21] on methods for function approximation had shown numerically that MQ outperformed all other tested functions, including other RBFs like thin plate splines and Gaussian. Therefore, all computations in the present work have been carried out with multiquadric (with $\nu = \frac{1}{2}$ and hence $m = 1$, from Table 1) as the radial function.

In RBF interpolation, a function is approximated as a linear combination of translates of a particular radial function $\phi(\|\cdot\|)$, which is radially symmetric about its center. In other words, for a given set of distinct nodes $\bar{x}_i \in \mathbb{R}^d$ and corresponding function values $u(\bar{x}_i)$, $i = 1, 2, \dots, n$, the RBF interpolant, $s(\bar{x})$, is of the form

$$u(\bar{x}) \approx s(\bar{x}) = \sum_{j=1}^n \lambda_j \phi(\|\bar{x} - \bar{x}_j\|) + \sum_{j=1}^l \gamma_j p_j(\bar{x}), \quad (1)$$

Table 1
Examples of certain radial functions

Name of the RBFs	$\phi(r)$, $r > 0$	Order of the RBF
Multiquadric (MQ)	$(1 + (\varepsilon r)^2)^\nu$, $\nu > 0$, $\nu \notin \mathbb{N}$	$m = \lceil \nu \rceil$
Inverse multiquadric (IMQ)	$(1 + (\varepsilon r)^2)^\nu$, $\nu < 0$	$m = 0$
Gaussian (GA)	$e^{-(\varepsilon r)^2}$	$m = 0$
Polyharmonic splines	$\begin{cases} r^\nu, & \nu > 0, \\ r^\nu \log(r), & \text{if } \nu \in 2\mathbb{N} - 1 \end{cases}$	$m = \begin{cases} \lceil \nu/2 \rceil \\ \nu/2 + 1 \end{cases}$

where $\|\cdot\|$ is the Euclidean norm and $\{p_j(\bar{x})\}_{j=1}^l$ is a basis for π_m^d (space of all d -variate polynomials with degree $< m$, where m is the order of ϕ and for multiquadric it is one). To take care of the extra degrees of freedom in (1), l extra conditions are necessary along with the interpolation conditions,

$$s(\bar{x}_i) = u(\bar{x}_i), \quad i = 1, \dots, n. \quad (2)$$

The extra l conditions are chosen by taking the coefficient vector $\lambda \in \mathbb{R}^n$ orthogonal to $\pi_m^d|_X$ (the polynomial space restricted to $X = \{\bar{x}_1, \bar{x}_2, \dots, \bar{x}_n\}$), i.e.,

$$\sum_{j=1}^n \lambda_j q(\bar{x}_j) = 0, \quad (3)$$

where $q \in \pi_m^d$.

Imposing the interpolation condition (2) and the condition (3) on $s(\bar{x})$, gives a linear system,

$$\begin{pmatrix} \Phi & p \\ p^T & \mathbf{0} \end{pmatrix} \begin{pmatrix} \lambda \\ \gamma \end{pmatrix} = \begin{pmatrix} \mathbf{u} \\ \mathbf{0} \end{pmatrix}, \quad (4)$$

where $\Phi_{ij} = \phi(\|\bar{x}_i - \bar{x}_j\|)$, $i, j = 1, \dots, n$ and $p_{ij} = p_j(\bar{x}_i)$, $j = 1, \dots, l$ and $i = 1, \dots, n$. The coefficient matrix in (4) is denoted as A for future reference.

2.2. Lagrange representation of RBF interpolation

To derive the RBF based 'local' scheme, Lagrange representation of the RBF interpolant is being considered, i.e., the interpolant is represented in the form,

$$s(\bar{x}) = \sum_{j=1}^n \psi_j(\bar{x}) u(\bar{x}_j), \quad (5)$$

where $\psi_j(\bar{x})$'s satisfy the cardinal conditions,

$$\psi_j(\bar{x}_k) = \delta_{jk}, \quad j, k = 1, 2, \dots, n. \quad (6)$$

The closed form representation for $\psi_j(\bar{x})$, in terms of $\phi(\|\bar{x} - \bar{x}_j\|)$'s, can be obtained by posing another set of RBF interpolation problems for which the data is obtained from the cardinal conditions on ψ_j , i.e., for each ψ_j the corresponding right hand side vector is e_j , the standard unit vector with j th component is 1 and rest are zeroes. Then, for each j , there will be a linear system which can be expressed in the form,

$$\begin{pmatrix} \phi_{11} & \dots & \phi_{1n} & p_{11} \\ \dots & \dots & \dots & \dots \\ \phi_{j1} & \dots & \phi_{jn} & p_{1j} \\ \dots & \dots & \dots & \dots \\ \phi_{n1} & \dots & \phi_{nn} & p_{1n} \\ p_{11} & \dots & p_{1n} & 0 \end{pmatrix} \begin{pmatrix} \lambda_{j1} \\ \dots \\ \lambda_{jj} \\ \dots \\ \lambda_{jn} \\ \gamma_{j1} \end{pmatrix} = \begin{pmatrix} \psi_j(\bar{x}_1) = 0 \\ \dots \\ \psi_j(\bar{x}_j) = 1 \\ \dots \\ \psi_j(\bar{x}_n) = 0 \\ 0 \end{pmatrix}, \quad (7)$$

where $\phi_{ij} = \phi(\|\bar{x}_i - \bar{x}_j\|)$, $i, j = 1, \dots, n$ and $p_{1j} = p_1(\bar{x}_j)$, $j = 1, \dots, n$. By Cramer's rule, for each λ_{jk} , $k = 1, \dots, n$ can be written as,

$$\lambda_{jk} = \frac{\det \begin{pmatrix} \phi_{11} & \dots & 0 & \dots & \phi_{1n} & p_{11} & \dots & p_{m1} \\ \dots & \dots & \dots & \dots & \dots & \dots & \dots & \dots \\ \phi_{j1} & \dots & 1 & \dots & \phi_{jn} & p_{1j} & \dots & p_{mj} \\ \dots & \dots & \dots & \dots & \dots & \dots & \dots & \dots \\ \phi_{n1} & \dots & 0 & \dots & \phi_{nn} & p_{1n} & \dots & p_{mn} \\ p_{11} & \dots & 0 & \dots & p_{1n} & 0 & \dots & 0 \\ \dots & \dots & \dots & \dots & \dots & \dots & \dots & \dots \\ p_{m1} & \dots & 0 & \dots & p_{mn} & 0 & \dots & 0 \end{pmatrix}}{\det \begin{pmatrix} \phi_{11} & \dots & \phi_{1k} & \dots & \phi_{1n} & p_{11} & \dots & p_{m1} \\ \dots & \dots & \dots & \dots & \dots & \dots & \dots & \dots \\ \phi_{j1} & \dots & \phi_{jk} & \dots & \phi_{jn} & p_{1j} & \dots & p_{mj} \\ \dots & \dots & \dots & \dots & \dots & \dots & \dots & \dots \\ \phi_{n1} & \dots & \phi_{nk} & \dots & \phi_{nn} & p_{1n} & \dots & p_{mn} \\ p_{11} & \dots & p_{1k} & \dots & p_{1n} & 0 & \dots & 0 \\ \dots & \dots & \dots & \dots & \dots & \dots & \dots & \dots \\ p_{m1} & \dots & p_{mk} & \dots & p_{mn} & 0 & \dots & 0 \end{pmatrix}}, \quad (8)$$

γ_{j1} also can be written in a similar fashion. Then, using λ_{jk} 's and γ_{j1} , each ψ_j can be written in terms of ϕ as

$$\psi_j(\bar{x}) \approx \sum_{k=1}^n \lambda_{jk} \phi(\|\bar{x} - \bar{x}_k\|) + \gamma_{j1} p_1(\bar{x}), \quad j = 1, 2, \dots, n \quad (9)$$

and then making use of some simple properties of determinants on Eq. (9) along with the symmetry of RBF interpolation matrix yields,

$$\psi_j(\bar{x}) = \frac{\det(A_j(\bar{x}))}{\det(A)}, \quad j = 1, 2, \dots, n, \quad (10)$$

where $A_j(\bar{x})$ is same as the matrix A , except that j th row is now replaced by the vector,

$$B(\bar{x}) = [\phi(\|\bar{x} - \bar{x}_1\|) \phi(\|\bar{x} - \bar{x}_2\|) \dots \phi(\|\bar{x} - \bar{x}_n\|) | p_1(\bar{x})], \quad (11)$$

where $p_1(\bar{x}) \in \Pi_1^d$.

2.3. RBF approximation of operators

The formulae derived in (5)–(11) can be used to approximate derivatives of a function or in general, value of $\mathcal{L}u$ at a certain point, say \bar{x}_i , where \mathcal{L} is a linear differential operator. To approximate $\mathcal{L}u(\bar{x}_i)$, consider a set S_i , consisting of n_i neighboring nodes of \bar{x}_i , given by $S_i = \{\bar{x}_1, \dots, \bar{x}_{n_i}\}$. Let $\mathcal{L}u(\bar{x}_i)$ be represented as a linear combination of u at the points of S_i , given by

$$\mathcal{L}u(\bar{x}_i) \approx \sum_{j=1}^{n_i} c_j u(\bar{x}_j). \quad (12)$$

Then, the computation of the weights c_j gives the required approximation to $\mathcal{L}u(\bar{x}_i)$. Applying the operator \mathcal{L} to the Lagrange representation of RBF interpolant in (5) gives,

$$\mathcal{L}u(\bar{x}_i) \approx \mathcal{L}s(\bar{x}_i) = \sum_{j=1}^{n_i} \mathcal{L}\psi_j(\bar{x}_i) u(\bar{x}_j). \quad (13)$$

From Eqs. (12) and (13), c_j 's can be obtained as,

$$c_j = \mathcal{L}\psi_j(\bar{x}_i), \quad j = 1, \dots, n_i. \quad (14)$$

For example, with $n_i = 3$ and $m = 1$, weights can have the expression of the form,

$$c_1 = \frac{\begin{vmatrix} \mathcal{L}\phi(\|\bar{x} - \bar{x}_1\|) & \mathcal{L}\phi(\|\bar{x} - \bar{x}_2\|) & \mathcal{L}\phi(\|\bar{x} - \bar{x}_3\|) & \mathcal{L}(1) \\ \phi_{21} & \phi_{22} & \phi_{23} & 1 \\ \phi_{31} & \phi_{32} & \phi_{33} & 1 \\ 1 & 1 & 1 & 0 \end{vmatrix}}{\begin{vmatrix} \phi_{11} & \phi_{12} & \phi_{13} & 1 \\ \phi_{21} & \phi_{22} & \phi_{23} & 1 \\ \phi_{31} & \phi_{32} & \phi_{33} & 1 \\ 1 & 1 & 1 & 0 \end{vmatrix}}$$

and so on, where the numerator is $\mathcal{L}[|A_1(\bar{x})|]$ and the denominator is $|A|$ as mentioned in (10) for c_1 .

Now, by making use of the symmetry of the interpolation matrix and applying Cramer's rule to (14), c_j 's can be obtained by solving the linear system,

$$\begin{pmatrix} \Xi & \mathbf{p} \\ \mathbf{p}^T & \mathbf{0} \end{pmatrix} \begin{pmatrix} \bar{c} \\ \bar{\mu} \end{pmatrix} = (\mathcal{L}B(\bar{x}_i)), \quad (15)$$

where $B(\bar{x})$ is the vector given in (11), $\bar{\mu}$, a dummy vector corresponding to the vector $\bar{\gamma}$ in (1) and Ξ and \mathbf{p} are as given in (4).

It is clear from the development of the final linear system (15) that though it is dense, the size of (15) is only n_i , which is very much smaller than the size (n) of the global RBF collocation system. This makes the system more stable for a wide range of ε . Moreover, only right hand side of (15) depends on the operator \mathcal{L} , for which the weights are to be computed. This property helps when weights are to be computed for many operators with same distribution of nodes, as in the case of nonlinear equations.

2.4. Algorithm

Consider a linear boundary value problem,

$$\left. \begin{aligned} \mathcal{L}u(\bar{x}) &= f(\bar{x}), \quad \text{if } \bar{x} \in \Omega, \\ \mathcal{B}u(\bar{x}) &= \alpha_1 u(\bar{x}) + \alpha_2 \frac{\partial u(\bar{x})}{\partial n} = g(\bar{x}), \quad \text{if } \bar{x} \in \partial\Omega. \end{aligned} \right\} \quad (16)$$

Let us assume that the domain is discretized with $n = n_I + n_B$ (n_I interior and n_B boundary) nodes. For each node $\bar{x}_i, i = 1, \dots, n$, assume that n_i nodes are used in the support domain, then the local RBF gridfree algorithm can be implemented using the following algorithm

- (1) Obtain the weights c_i for each node $\bar{x}_i, i = 1, \dots, n$ by solving Eq. (15), with right hand side as $\mathcal{L}(B(\bar{x}))_{\bar{x}_i}$, if $\bar{x}_i \in \Omega$ or $\mathcal{B}(B(\bar{x}))_{\bar{x}_i}$, if $\bar{x}_i \in \partial\Omega$, where $B(\bar{x})$ is the vector given in (11).
- (2) Assemble the weights at the proper locations, depending on the nodes of the set S_i , in the i th row of the global matrix \mathbf{L} .
- (3) Solve the global system using any iterative method (for most of the iterative solvers explicit generation of global matrix \mathbf{L} may not be needed).

3. Local RBF based gridfree scheme to transient incompressible Navier–Stokes equations

The transient incompressible Navier–Stokes equations, in non-dimensional form, are

$$\text{Continuity equation : } \nabla \cdot \bar{V} = 0, \quad (17)$$

$$\text{Momentum equations : } \frac{\partial \bar{V}}{\partial t} + (\bar{V} \cdot \nabla) \bar{V} = -\nabla P + \frac{1}{Re} \nabla^2 \bar{V}, \quad (18)$$

where $\bar{V} = (u_{e_1}, \dots, u_{e_d})$ is the velocity field, $\nabla = e_j \frac{\partial}{\partial x_{e_j}}$ is the gradient operator, $\nabla^2 = \frac{\partial^2}{\partial x_{e_j} \partial x_{e_j}}$ is the Laplacian operator, $j = 1, 2, \dots, d$, d is the dimension of the problem, P is the pressure and Re is the dimensionless parameter called Reynolds number defined by $Re = \frac{Ul}{\nu}$, U is the characteristic velocity, l is the characteristic length and ν is the kinematic viscosity. The necessary initial and boundary conditions depend on the chosen problem and will be discussed later.

The procedure, described in this section, is based on the explicit Euler time discretization. The development of the scheme based on other temporal schemes also can be generated, however, for simplicity Euler scheme has been chosen in the presentation.

Discretization of the momentum equation (18) by Euler method gives

$$\frac{\bar{V}^{(n+1)} - \bar{V}^{(n)}}{\Delta t} = -(\bar{V}^{(n)} \cdot \nabla) \bar{V}^{(n)} - \nabla P^{(n)} + \frac{1}{Re} \nabla^2 \bar{V}^{(n)} \quad (19)$$

(or)

$$\bar{V}^{(n+1)} = \bar{V}^{(n)} + \Delta t \left[-(\bar{V}^{(n)} \cdot \nabla) \bar{V}^{(n)} - \nabla P^{(n)} + \frac{1}{Re} \nabla^2 \bar{V}^{(n)} \right]. \quad (20)$$

Rewriting (20) in the form

$$\bar{V}^{(n+1)} = \bar{V}^* + \Delta t (-\nabla P^{(n)}), \quad (21)$$

where \bar{V}^* , computed from (20), can be given as

$$\bar{V}^* = \bar{V}^{(n)} + \Delta t \left[-(\bar{V}^{(n)} \cdot \nabla) \bar{V}^{(n)} + \frac{1}{Re} \nabla^2 \bar{V}^{(n)} \right]. \quad (22)$$

At each time step, the solution is expected to satisfy continuity equation. Hence $\bar{V}^{(n+1)}$ must satisfy the continuity equation (17), which implies

$$\nabla \cdot \bar{V}^{(n+1)} = 0 \quad (\text{or}) \quad \nabla \cdot (\bar{V}^* - \Delta t \nabla P^{(n)}) = 0. \quad (23)$$

Eq. (23) can be simplified to

$$\nabla^2 P^{(n)} = \frac{1}{\Delta t} \nabla \cdot \bar{V}^*. \quad (24)$$

Eq. (24) is a Poisson's equation with non-zero source term $\frac{1}{\Delta t} \nabla \cdot \bar{V}^*$ (\bar{V}^* may not satisfy continuity equation). Numerical implementation of the procedure described from (19) to (24) can be summarized as follows.

3.1. Numerical algorithm

At every time step,

- (1) Compute intermediate velocity field $\bar{V}^* = (u_{e_1}^*, \dots, u_{e_d}^*)$ using

$$\bar{V}^* = \bar{V}^{(n)} + \Delta t \left[-(\bar{V}^{(n)} \cdot \nabla) \bar{V}^{(n)} + \frac{1}{Re} \nabla^2 \bar{V}^{(n)} \right]. \quad (25)$$

- (2) Solve the pressure Poisson's equation,

$$\nabla^2 P^{(n)} = \frac{1}{\Delta t} \nabla \cdot \bar{V}^*, \quad \text{BC} : \frac{\partial p^{(n)}}{\partial \bar{n}} = \frac{1}{\Delta t} (\bar{V}^* - \bar{V}^{(n)}). \quad (26)$$

(3) Update the velocity field to $(n+1)$ th time level using

$$\bar{V}^{(n+1)} = \bar{V}^* + \Delta t (-\nabla P^{(n)}). \quad (27)$$

The above algorithm can be implemented using radial basis functions as follows. Since $\bar{V}^{(n)}$ is known, the right hand side of (25) can be taken as $\mathcal{L}\bar{V}^{(n)}$, where $\mathcal{L} = -(\bar{V}^{(n)} \cdot \nabla) + \frac{1}{Re} \nabla^2$. Then compute the weights using (15) with right hand side as $\mathcal{L}B(\bar{x}_i)$, which is evaluated using (11). Finally, $\mathcal{L}\bar{V}^{(n)}$ is obtained using (12). To compute each component of \bar{V} , the above procedure is repeated for d number of times, where d is the dimension of the problem.

The pressure Poisson equation (Neumann problem) in Step (2) is solved using the Algorithm 2.4. The linear system, in the third step of the Algorithm 2.4, is solved using either SOR or Bi-CGSTAB without explicitly storing the matrix \mathbf{L} .

The gradient of the pressure in Step 3 is computed in a similar manner as the operator \mathcal{L} in Step 1, except that the operator is now the gradient operator ∇ .

4. Validation of the scheme

In this section, the developed RBF scheme, described in the previous section, is validated by solving some fluid flow problems. Popular laminar flow problems like Couette and Poiseuille flows and complex flow problems like lid driven cavity and backward-facing step problems are considered for validation. Finally, the validated code is used to solve the stenosis problem, that is, the blood flow through arteries with a local constriction.

For all the chosen test problems, steady state solutions have been obtained through unsteady computations. The steady state is assumed to be achieved whenever the relative error satisfies,

$$\max \left| \frac{(\hat{u}^{(n+1)} - \hat{u}^{(n)})}{\hat{u}^{(n)}} \right| < \text{tol}_{\text{st}}, \quad (28)$$

where $\hat{u}^{(n)}$ and $\hat{u}^{(n+1)}$ are the computed solutions at n th and $(n+1)$ th time levels, respectively. tol_{st} is the steady state error tolerance and its value has been fixed as 10^{-06} .

The laminar viscous flow problems like Couette and Poiseuille flows are some simple problems in incompressible viscous flows. The square or rectangular geometry and the availability of analytical solutions make these problems useful in the validation of any numerical scheme. Therefore, these problems have been chosen for testing the developed 'local' RBF scheme. The obtained results have been compared with the corresponding analytical solutions. Due to the existence of analytical solutions for these two problems, the developed RBF scheme has been tested on them by varying the value of the multiquadric shape parameter ε and support domains to study their effect on the accuracy.

4.1. Couette flow

Couette flow is a laminar flow of a viscous fluid in the space between two surfaces, one of which is moving relative to the other. It is perhaps the simplest of all viscous flows, while at the same time retaining many of the physical characteristics of a complicated boundary layer flow and also represents the exact analytical solution of the Navier–Stokes equations.

Couette flow can be defined by considering a viscous flow between two parallel plates separated by a unit vertical distance, as given in the Fig. 1. The upper plate is moving with a constant velocity one (non-dimensionalized) and the lower plate is stationary. The flow is driven by virtue of viscous drag force acting on the fluid, as shown in Fig. 1. The analytical solution of the described Couette flow is

$$u(y, t) = y + \frac{2}{\pi} \sum_{k=1}^{\infty} \frac{(-1)^k}{k} \sin(k\pi y) e^{-\frac{k^2 \pi^2}{Re} t} \quad (29)$$

from which the initial and boundary conditions are taken.

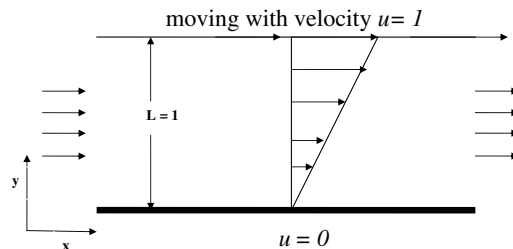


Fig. 1. Schematic of Couette flow.

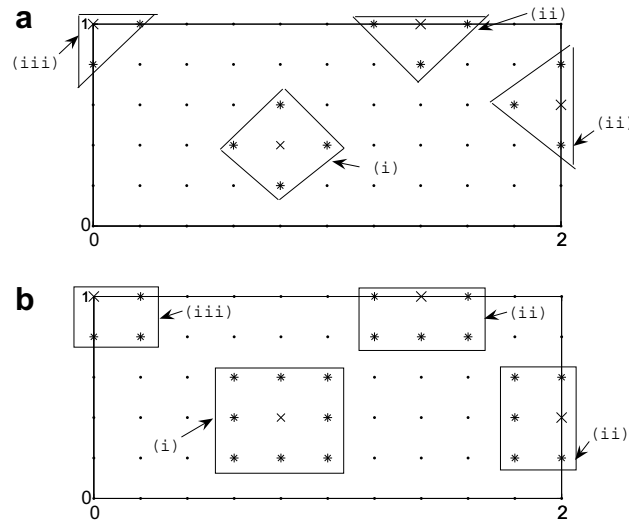


Fig. 2. Discretization of the domain for Couette flow with (a) 5-node, (b) 9-node support domains: (i) internal, (ii) boundary and (iii) corner nodes.

To solve Couette flow using the developed RBF scheme, the computational domain (Fig. 2) has been fixed as $[0, 2] \times [0, 1]$ for (x, y) and the steady state solutions have been obtained using different uniform nodal distributions with nodal spacing varied from 0.2 to 0.025. Since the laminar flow is valid only for very low Reynolds' numbers, present computations have been carried out with $Re = 1$. The time step Δt has been varied from 0.001 to 0.00001 to obtain stable solutions using Euler method. The time step has been made deliberately low so that the time discretization errors do not dominate the errors of space discretization which has been realised using RBFs.

Fig. 2 gives the discretization of the domain and the choice of two different support domains used in the simulations. Both 5-node and 9-node supports have been considered and the supports for boundary and corner nodes have been taken accordingly.

Both initial and boundary conditions for velocities have been taken from the available analytical solution. For pressure, boundary conditions are constructed from (21). SOR iterative solver with the pressure at (n) th time level as the initial approximation has been used to solve the pressure Poisson equation. The pressure iterative process is also been carried out with Bi-CGSTAB, however, not much reduction in the CPU time is observed.

Velocity profiles at various time levels have been compared with the corresponding analytical solutions and presented in Fig. 3. Table 2 reports the errors with respect to infinity norm (err_∞). The fourth to tenth decimal place accuracy in these results demonstrates the robustness of the local RBF scheme. These solutions are obtained with $\varepsilon = 1$.

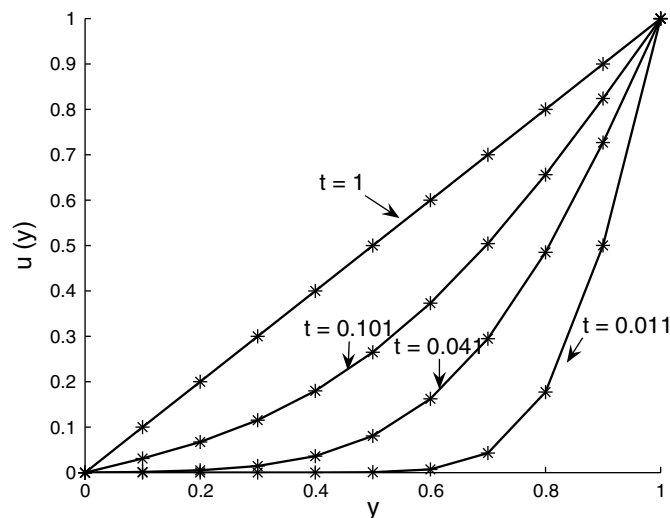


Fig. 3. Comparison of the velocity profiles at various time levels for Couette flow.

Table 2Error (err_∞) at different time levels for Couette flow

n	11×6	21×11	41×21	81×41
$t \Delta t \rightarrow$	0.001	0.0001	0.00005	0.00001
0.011	3.92(−02)	1.12(−02)	3.16(−03)	8.93(−04)
0.101	8.73(−04)	2.24(−04)	5.69(−05)	1.44(−05)
1.0	5.95(−08)	1.46(−08)	1.77(−09)	8.18(−10)

Table 3Error err_∞ at $t = 0.6$ for various values of ε on 41×21 nodes using 5-node and 9-node supports

ε	5-node support	9-node support
0.005	Diverged	Diverged
0.01	3.147(−07)	Diverged
0.05	1.670(−07)	Diverged
0.1	1.659(−07)	Diverged
0.2	1.581(−07)	Diverged
0.3	1.450(−07)	1.573(−07)
0.5	1.031(−07)	1.283(−07)
1	9.187(−08)	3.808(−09)
2	8.521(−07)	4.762(−07)
5	5.433(−06)	3.190(−06)
10	1.568(−05)	Diverged
15	Diverged	Diverged

Table 4Error err_∞ at $t = 1$ for various values of ε on 41×21 nodes using 5-node and 9-node supports

ε	5-node support	9-node support
0.005	Diverged	Diverged
0.01	6.073(−09)	Diverged
0.05	3.222(−09)	Diverged
0.1	3.202(−09)	Diverged
0.2	3.050(−09)	Diverged
0.3	2.797(−09)	3.035(−09)
0.5	1.989(−09)	2.475(−09)
1	1.772(−09)	7.349(−11)
2	1.644(−08)	9.188(−09)
5	1.048(−07)	6.154(−08)
10	3.026(−07)	Diverged
15	Diverged	Diverged

To see the effect of the shape parameter ε and the size of the support domain, solutions are also obtained for various values of shape parameter over 5-node and 9-node supports and the corresponding results are compared with the analytical solutions at $t = 0.6$ and $t = 1$. The obtained error norms are presented in [Tables 3 and 4](#), respectively. The steady state solution has been reached near 0.7 for both 5-node and 9-node supports with 10^{-06} error tolerance. For ε between 0.01 and 10, a converged solution has been obtained for 5-node support, however, with 9-node support converged solution could be obtained for ε only between 0.3 and 5. The divergence of the solution may be due to the stability restriction of the explicit Euler method. Also it can be observed from these comparisons that the solution accuracy has been improved with 9-node stencil nearly by an order, though this is not seen for smaller ε due to the ill-conditionness of the corresponding local matrix. Further, the solution seems to be more accurate near $\varepsilon = 1$.

4.2. Plane Poiseuille flow

Plane Poiseuille flow is another classical and simple problem in viscous, laminar flow involving the steady-state velocity and pressure distributions for a fluid moving laterally between two plates whose length and width are much greater than the distance separating them. The flow is driven by a pressure gradient in the direction of the flow, and is retarded by viscous drag along the two plates, such that these forces are in balance.

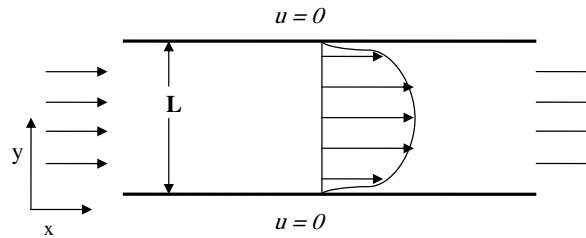


Fig. 4. Schematic of Poiseuille flow.

The flow can be described by considering a viscous flow between two stationary parallel plates separated by a unit vertical distance, as given in Fig. 4. For this specific problem, the velocity component and the pressure gradient in the vertical y -direction vanishes identically so that the x -component of the velocity depends only on y . Analytical solution of the plane Poiseuille flow is given by,

$$u(y, t) = \frac{Re}{2} y(y-1) + \frac{4Re}{\pi^3} \sum_{k=0}^{\infty} \frac{1}{(2k+1)^3} \sin \pi y (2k+1) e^{-\frac{(2k+1)^2 \pi^2}{Re} t}. \quad (30)$$

In this problem, initial and boundary conditions for velocity and the pressure boundary conditions have been taken in a similar way as that of Couette flow and the solutions have been obtained. The time step Δt has been varied from 0.001 to 0.00001 depending on the nodal density. Velocity profiles at various time levels have been compared with the corresponding analytical solution and presented in Fig. 5. Table 5 reports the errors (err_{∞}). A third to fifth decimal accuracy in the results again confirms the applicability of the developed scheme.

As in the case of Couette flow, dependence of ε has been tested again for Poiseuille flow using both 5-node and 9-node support domains (refer Tables 6 and 7). Steady state solutions have been reached for both the cases in the vicinity of $t = 0.63$. When compared with the results of Couette flow, a similar convergence behaviour is observed, though plane Poiseuille flow problem seems to be insensitive to ε and the size of the support.

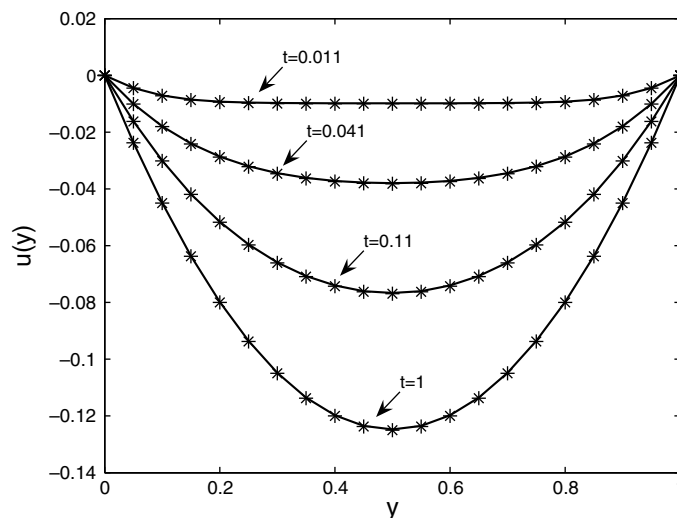


Fig. 5. Comparison of the velocity profiles at various time levels for Poiseuille flow.

Table 5

Error (err_{∞}) for at different time level for Poiseuille flow

n	11×6	21×11	41×21	81×41
$t \downarrow \Delta t \rightarrow$	0.001	0.0001	0.00005	0.00001
0.011	8.27(-03)	2.47(-03)	6.35(-04)	1.53(-04)
0.041	8.32(-03)	2.55(-03)	5.88(-04)	1.47(-04)
0.101	8.46(-03)	2.57(-03)	5.69(-04)	1.14(-04)
1.0	8.71(-03)	2.59(-03)	4.55(-04)	9.98(-05)

Table 6Error err_{∞} at $t = 0.6$ for various values of ε on 41×21 nodes using 5-node and 9-node supports

ε	5-node support	9-node support
0.005	Diverged	Diverged
0.01	3.1927(−04)	Diverged
0.05	3.1772(−04)	Diverged
0.1	3.1772(−04)	Diverged
0.2	3.1773(−04)	Diverged
0.3	3.1775(−04)	3.1509(−04)
0.5	3.1783(−04)	3.1536(−04)
1	3.1817(−04)	3.1549(−04)
2	3.1951(−04)	3.1599(−04)
5	3.2832(−04)	3.1857(−04)
10	3.5500(−04)	Diverged
15	Diverged	Diverged

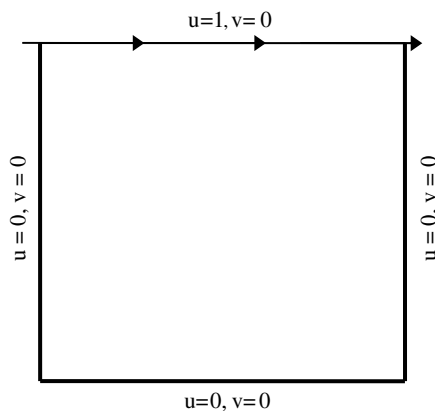
Table 7Error err_{∞} at $t = 1$ for various values of ε on 41×21 nodes using 5-node and 9-node supports

ε	5-node support	9-node support
0.005	Diverged	Diverged
0.01	3.1928(−04)	Diverged
0.05	3.1771(−04)	Diverged
0.1	3.1771(−04)	Diverged
0.2	3.1773(−04)	Diverged
0.3	3.1775(−04)	3.1509(−04)
0.5	3.1783(−04)	3.1536(−04)
1	3.1817(−04)	3.1549(−04)
2	3.1953(−04)	3.1600(−04)
5	3.2845(−04)	3.1862(−04)
10	3.5540(−04)	Diverged
15	Diverged	Diverged

From the results of these two problems, it can be seen that the dependance of the shape parameter and the support domain does not seem to have much impact on the accuracy. Hence, the value of ε has been fixed as one with the standard 5-node stencil as the support domain for the remaining problems.

4.3. Flow in a lid driven cavity

Lid driven cavity problem is one of the well-known bench mark problem, which is often used to test the numerical schemes. Despite its simple geometry, the driven cavity flow retains a rich physics of fluid flow manifested by multiple recirculating regions on the corners of the cavity depending on the value of Reynolds number.

**Fig. 6.** Schematic of lid driven cavity flow.

Schematic of the problem is given in Fig. 6, in which the cavity is defined in a square region $[0,1] \times [0,1]$. The flow is induced by the sliding motion of the top wall from left to right. No slip boundary conditions are considered on all the walls; i.e., on the top wall $u = 1$, $v = 0$, and on all other walls $u = 0$ and $v = 0$, as shown in Fig. 6.

Since the boundary values of velocity components are available, the boundary condition for pressure is again taken from the condition (21), which is essentially $\frac{\partial p}{\partial n} = 0$. The problem has been extensively studied for various Reynolds' numbers on

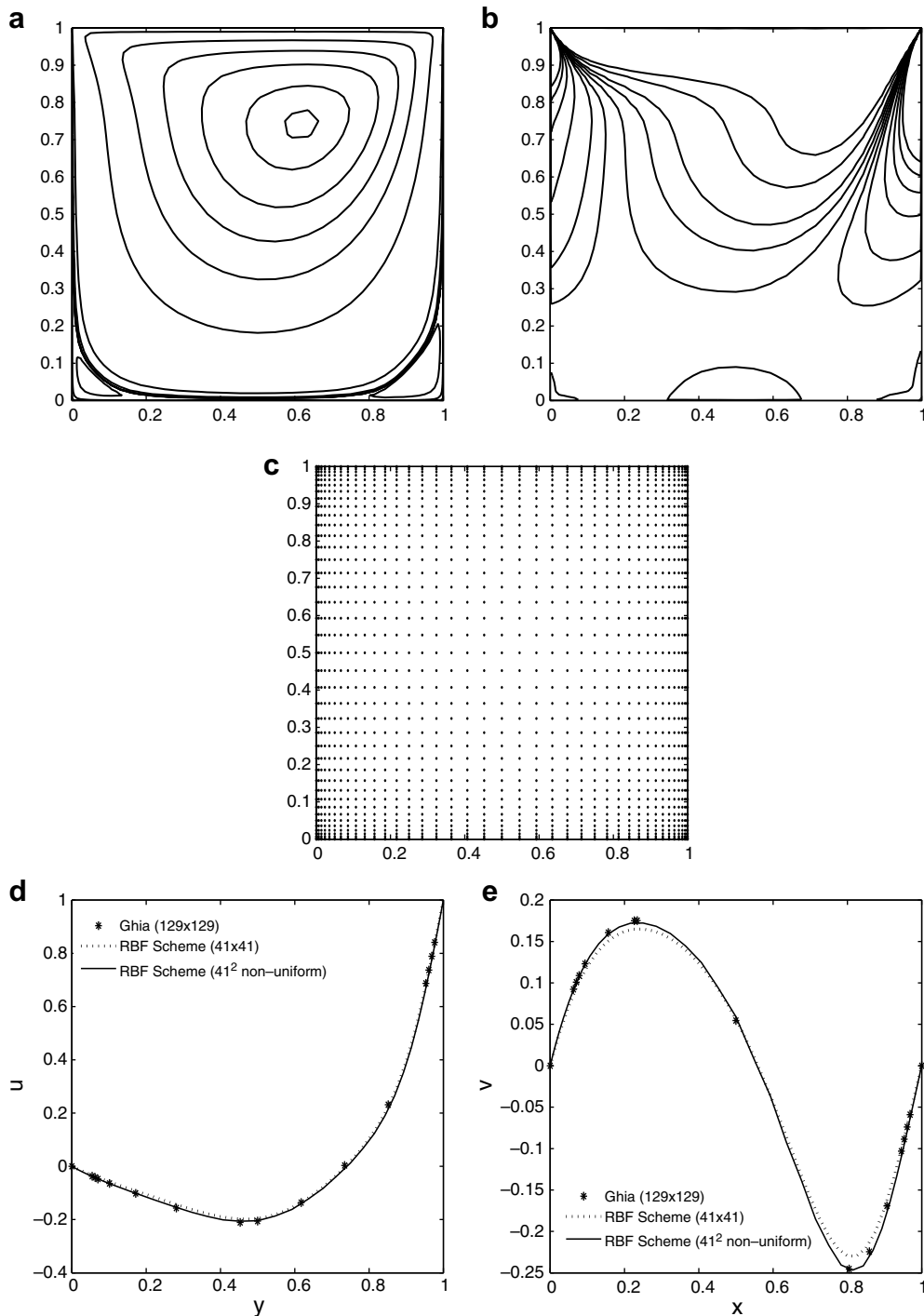


Fig. 7. At $Re = 100$: (a) streamlines, (b) vorticity contours, (c) 41×41 non-uniform nodal distribution, comparison of (d) u -velocity component along vertical line and (e) v -velocity component along horizontal line, passing through the geometric centre.

both uniform and non-uniform nodal distributions. The results for $Re = 100$, 1000 and 3200 are given in Figs. 7–9 and Tables 8–10, respectively.

The results have been presented by comparing velocity components (u, v) as well as stream function and vorticity (ψ, ω) values with the benchmark solutions from [22]. The computation of ψ and ω values has been performed as a post-computation using the velocity field by considering the following relationships between (ψ, ω) and (u, v),

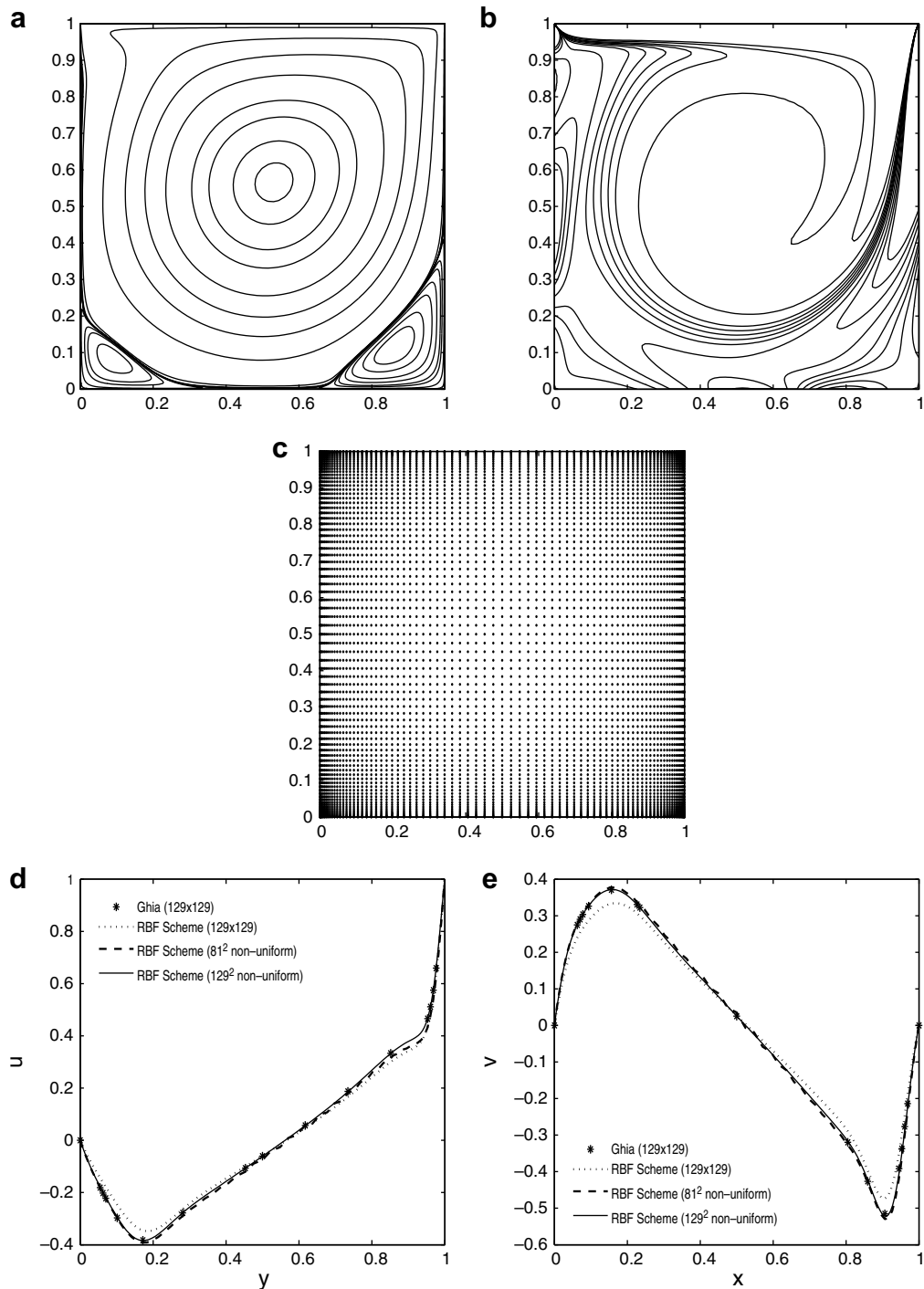


Fig. 8. At $Re = 1000$: (a) streamlines, (b) vorticity contours, (c) 81×81 non-uniform nodal distribution, comparison of (d) u -velocity component along vertical line and (e) v -velocity component along horizontal line, passing through the geometric centre.

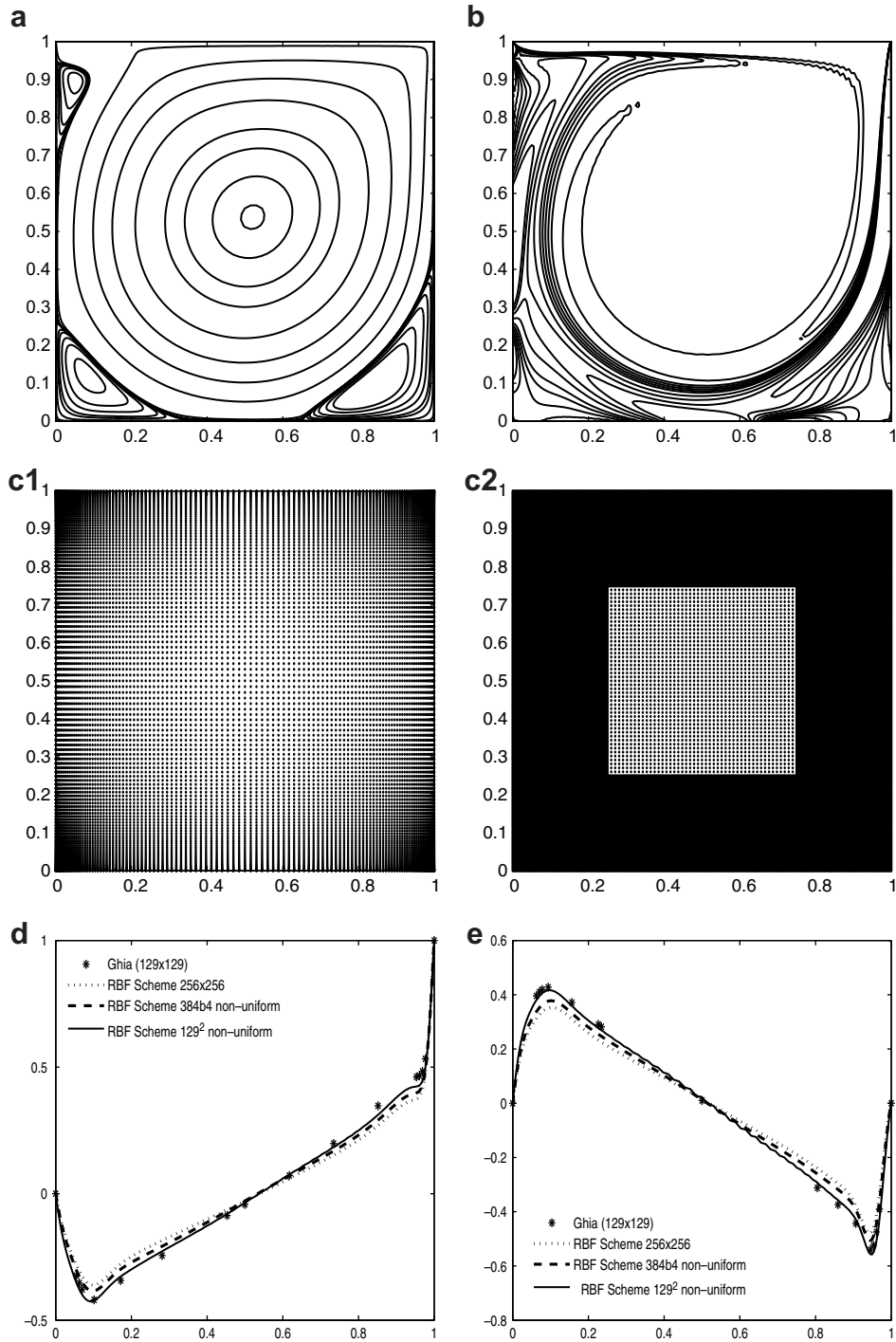


Fig. 9. At $Re = 3200$: (a) streamlines, (b) vorticity contours, (c1) 129×129 and (c2) 113953 non-uniform nodal distributions, Comparison of (d) u -velocity component along vertical line and (e) v -velocity component along horizontal line, passing through the geometric centre.

$$u = \frac{\partial \psi}{\partial y}, \quad v = -\frac{\partial \psi}{\partial x} \quad (31)$$

and

$$\omega = \frac{\partial v}{\partial x} - \frac{\partial u}{\partial y}. \quad (32)$$

Table 8

Comparison of centre of primary vortex and the corresponding stream function and vorticity values with [22]

Re	RBF scheme	Ghia et al.
100 (x, y)	0.6357, 0.7500	0.6172, 0.7344
ψ	−0.1013	−0.1034
ω	3.1047	3.1646
1000 (x, y)	0.5305, 0.5601	0.5313, 0.5625
ψ	−0.1164	−0.1179
ω	2.0389	2.0497
3200 (x, y)	0.5154, 0.5305	0.5165, 0.5469
ψ	−0.1155	−0.1204
ω	1.9991	1.9886

Table 9

Comparison of centre of secondary vortices and the corresponding stream function and vorticity values with [22]

Re	Right		Left	
	RBF scheme	Ghia et al.	RBF scheme	Ghia et al.
100 (x, y)	0.9333, 0.0667	0.9453, 0.0625	0.0500, 0.0500	0.0313, 0.0391
ψ	4.38(−05)	1.52(−05)	2.05(−05)	1.75(−06)
ω	−5.49(−02)	−3.31(−02)	−3.97(−02)	−1.56(−02)
1000 (x, y)	0.8651, 0.1118	0.8594, 0.1094	0.0909, 0.0781	0.0859, 0.0781
ψ	1.96(−03)	1.75(−03)	3.68(−04)	2.31(−04)
ω	−1.0862	−1.1546	−0.3899	−0.3617
3200 (x, y)	0.8310, 0.0844	0.8125, 0.0859	0.0844, 0.1118	0.0859, 0.1094
ψ	3.00(−03)	3.14(−03)	1.13(−03)	9.78(−04)
ω	−2.0786	−2.2736	−1.0112	−1.0630

Table 10

Comparison of centre of top left secondary vortex and the corresponding stream function and vorticity values with [22]

Re	RBF scheme	Ghia et al.
3200 (x, y)	0.0555, 0.8954	0.0547, 0.8984
ψ	6.87(−04)	7.28(−04)
ω	−1.6375	−1.7116

Substituting (31) in (32) gives,

$$\frac{\partial^2 \psi}{\partial x^2} + \frac{\partial^2 \psi}{\partial y^2} = -\omega. \quad (33)$$

After computing ω using (32), Eq. (33) is solved iteratively with appropriate boundary conditions for ψ . Eq. (31) and the boundary conditions of u and v on the walls implies that ψ must be a constant on all these walls. In all the computations this constant has been taken as zero. The same procedure given through (31)–(33) has been used for $\psi - \omega$ computation for all the test problems.

In Figs. 7–9, the subfigures (a) and (b) depict the stream lines and iso-vorticity contours, respectively. A non-uniform distribution of nodal points, as given in subfigure (c) of all the figures, has been used in these computations. The number of nodes (non-uniform) in the domain have been fixed as $n = 41 \times 41$ for $Re = 100$ and $n = 129 \times 129$ for $Re = 1000$ and 3200. All these figures demonstrate the typical separation and formation of secondary vortices at the bottom corners of the cavity as well as at the top left, for 3200, of the square cavity. The location of the centre of primary and secondary vortices and the corresponding stream function and vorticity values at these centres have been compared, with the available benchmark data given by Ghia et al. [22], in Tables 8–10 for $Re = 100$, 1000 and 3200, respectively. Both results agree up to 2nd significant digit.

A second quantitative assessment is made by comparing the velocity components through the geometric centre (g.c.) of the cavity. The results have been compared with [22] for various nodal distributions. For high Reynolds's numbers, the accuracy in the results has been improved by using more denser nodal distributions in the corners. For example, it can be seen from (d) and (e) of Fig. 9 that the non-uniform 129×129 distribution of nodes gave more accurate results compared to the corresponding 129×129 uniform distribution. A distribution of nodes as given in Fig. 9(c2) (113,953 nodes) has also been considered, in which a very fine (1/384) distribution near boundary and a coarse (1/96) distribution elsewhere has been ta-

ken. However, the non-uniform 129×129 based results are found to be more accurate. The better accuracy using 129×129 distribution is may be due to the continuous variation of the nodes, which is not the case for the distribution given in Fig. 9(c2). For both uniform and non-uniform distributions computations have been performed using a 5-node support (chosen in a similar fashion as in the previous test problems) with $\varepsilon = 1$.

In these studies, time step Δt has been taken as 0.0005 and 0.00005, respectively for 41×41 uniform and non-uniform cases. Time step Δt is taken as 0.0005 for 129×129 uniform distribution, while $\Delta t = 0.00001$ for 81×81 and 129×129 non-uniform distributions. For the case as given in Fig. 9(c2), Δt is taken as 0.0001. For $Re = 100$, 1000 and 3200, the steady state solutions have been reached approximately around $t = 20$, 40 and 65.

4.4. Flow over a backward-facing step

Two dimensional laminar incompressible flow over a backward-facing step (BFS) has been one of the standard benchmark problems to test the ability of newly developed numerical methods in predicting the flow separation and reattachments accurately. Typical flows around buildings or large structures where flow separation occurs when the flow passes over sharp corners of the building and its reattachment far downstream can be considered as one of the practical examples of such flows. The presence of separated flow, together with flow reattachment, can cause increased unsteadiness, pressure load, structural vibrations and noise. Understanding the flow around buildings or large structures is of vital importance to make a better design.

Many numerical studies on the two dimensional incompressible flow over a backward-facing step can be found in the literature. Kaiktsis et al. [23], in their computations, using spectral element method, claimed that the flow at $Re = 800$ is unsteady and exhibits chaotic nature. Runchal [24] and Choudhury [25] also have come up with a similar conclusion with the computations using some unsteady finite volume methods. However, these results went against the benchmark solutions provided by Gartling [26] in which the author obtained the solutions through steady computations assuming the existence of steady solution. To establish the reality, Gresho et al. [27] have made a joint effort by considering variety of numerical methods, like finite element, finite difference and spectral element, and obtained steady and stable solutions at $Re = 800$ through unsteady computations.

Some of the other investigations include, [19,28–31], in which the authors have studied the BFS flow for Reynolds' numbers varying up to 800. Cruchaga [32] solved the steady BFS flow using finite element method and obtained steady numerical solutions up to $Re = 5500$, although $Re = 800$ has been their primary interest. Apart from these studies, Ramsak and Skerget [33] has obtained solutions for steady flow over a BFS for $Re = 1000$.

This shows the wide attention received for the BFS problem at $Re = 800$ by numerous investigators in the literature. The controversy in obtaining the steady flow through unsteady computations at $Re = 800$ makes the problem challenging and hence, in the present study, the Reynolds' number Re has been fixed as 800.

As shown in Fig. 10, the downstream channel is defined to have a unit height H , with a step height and inlet region heights set equally to $H/2$ with the solution domain corresponds to the geometry of the benchmark case given in Gartling [26]. No slip boundary conditions have been set at all the solid surfaces, while a parallel flow with a parabolic horizontal component, given by $u(y) = 24y(0.5 - y)$, has been specified at the inlet $0 \leq y \leq 0.5$.

Detailed studies were made on the effect of different outflow boundary conditions (OBCs) for incompressible flows at two *Minisymposiums on Outflow Boundary Conditions*. In the report by Sani and Gresho [31], they have investigated various OBCs which include pseudo stress-free condition,

$$-P + \frac{1}{Re} \frac{\partial u}{\partial x} = 0, \quad \frac{\partial v}{\partial x} = 0 \quad (34)$$

and true stress-free condition,

$$-P + \frac{2}{Re} \frac{\partial u}{\partial x} = 0, \quad \frac{\partial u}{\partial y} + \frac{\partial v}{\partial x} = 0. \quad (35)$$

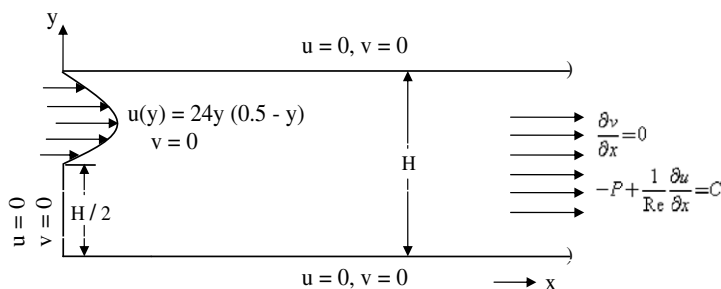


Fig. 10. Schematic of the flow over a backward-facing step.

Sani and Gresho [31], in their paper remarked that although the physical interpretation of the condition in (34) is not clear, it is preferred over the stress-free condition in (35), since all the stresses do not necessarily vanish at an outflow boundary. Therefore, in the present computations, conditions given in (34) have been used.

The differential equations in (34) have been incorporated in the RBF based fractional step approach in the following manner: (i) The natural pressure boundary conditions in (26) are replaced with $-P + \frac{1}{Re} \frac{\partial u}{\partial x} = 0$; (ii) momentum equations are forced to satisfy $\frac{\partial v}{\partial x} = 0$ at the outlet.

Uniform nodal distribution has been considered with two different nodal spacings 0.025 and 0.0125 with time step as 0.0001. Like in the earlier cases standard 5-point stencil has been chosen as support domain. The initial conditions for the flow have been taken by simply extending the boundary conditions at $x = 0$ throughout the channel, so that the initial condition satisfy the incompressibility constraint. Since pressure values at the outflow boundary can be computed using (34), Neumann boundary condition (26) has been taken only on the rest of the boundaries. As mentioned before, the value of the shape parameter ε has been fixed as one in all these computations.

Streamline plots have been given in Figs. 11 and 12 to illustrate the recirculating regions occur in the backward-facing step. The streamline patterns obtained by Gresho et al. [27] are also included in these figures for the sake of qualitative comparison. It can be observed that at around time $t = 30$ the small eddies which were present earlier have been disappeared and only two large eddies on upper and lower walls appear to be present. However, the steady state has been reached only around $t = 400$ and both the eddies have been stretched and shifted towards the downstream from their locations at $t = 30$. The streamlines and iso-vorticity contours of the steady state solution have been compared with Gresho et al. [27] in Fig. 13.

To verify the long term behaviour of the solutions, time history plots for the x -component of the velocity at different cross-sections of the channel have been given in Fig. 14 for various vertical positions. Oscillatory behaviour shown in the

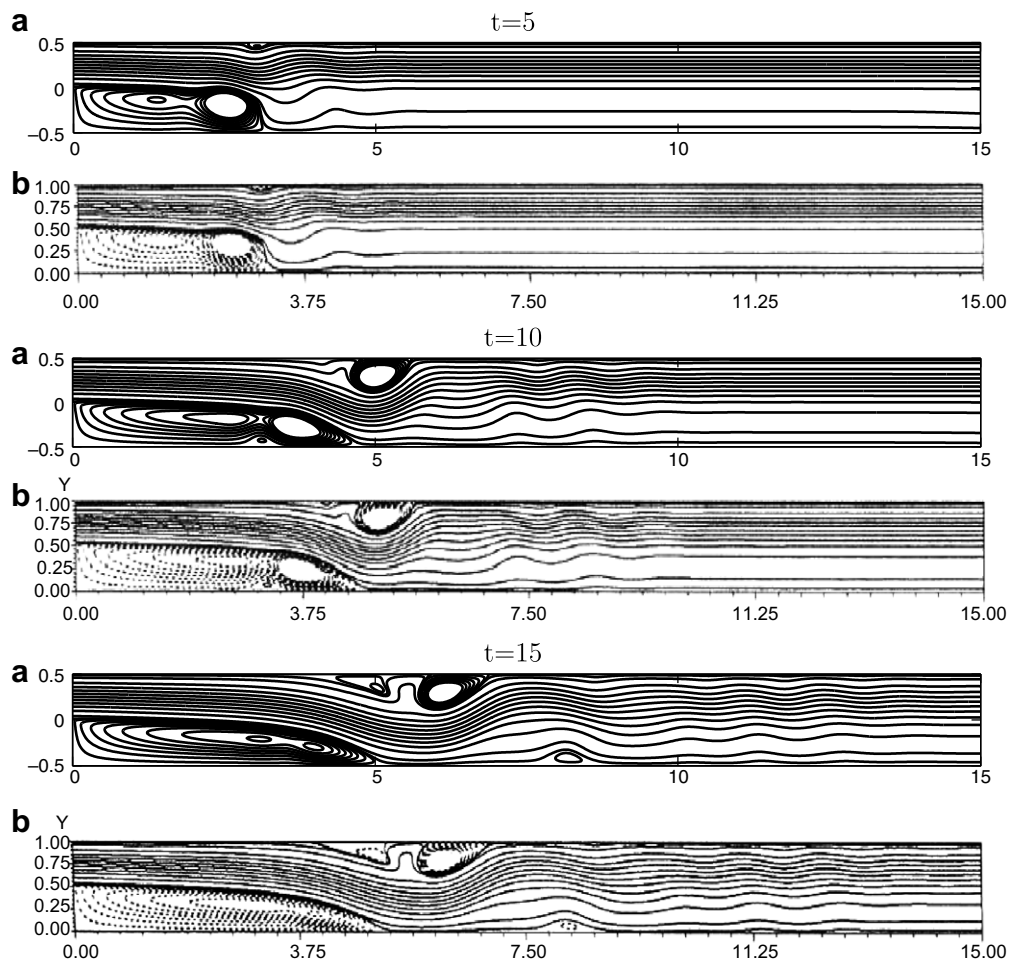


Fig. 11. Development of the flow over a backward-facing step – streamlines; (a) present; (b) [27].

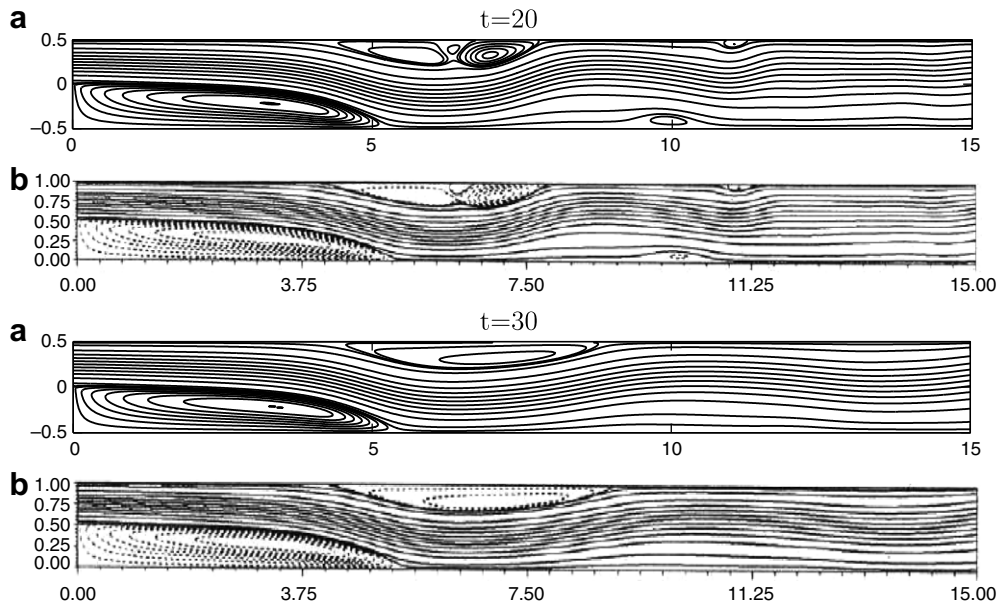


Fig. 12. Development of the flow over a backward-facing step – streamlines; (a) present; (b) [27].

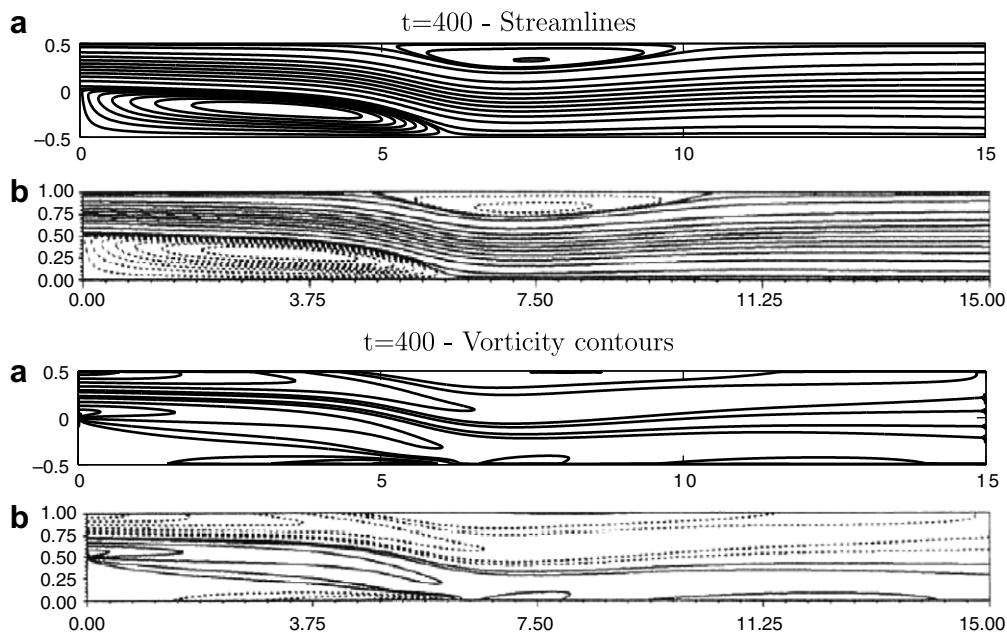


Fig. 13. Steady state solution of the flow over a backward-facing step – streamlines and vorticity contours: (a) present; (b) [27].

initial time, approximately up to $t = 60$, describes the formation and breakdown of the eddies. After this time, visually there is no disturbances which shows the convergence of the steady state solution.

A quantitative comparison of the solution has been done by comparing the velocity components, pressure and vorticity using the benchmark solutions of Gartling [26] and shown in Fig. 15. The results obtained using different nodal densities have been included in all these comparisons. From these comparisons, it can be seen that the solutions are in excellent agreement with that of Gartling [26].

Streamfunction–vorticity values have been computed by the same procedure discussed through Eqs. (31)–(33). Boundary condition for stream function at the inlet is obtained by integrating the u -component of the velocity. Then, at solid walls, ψ

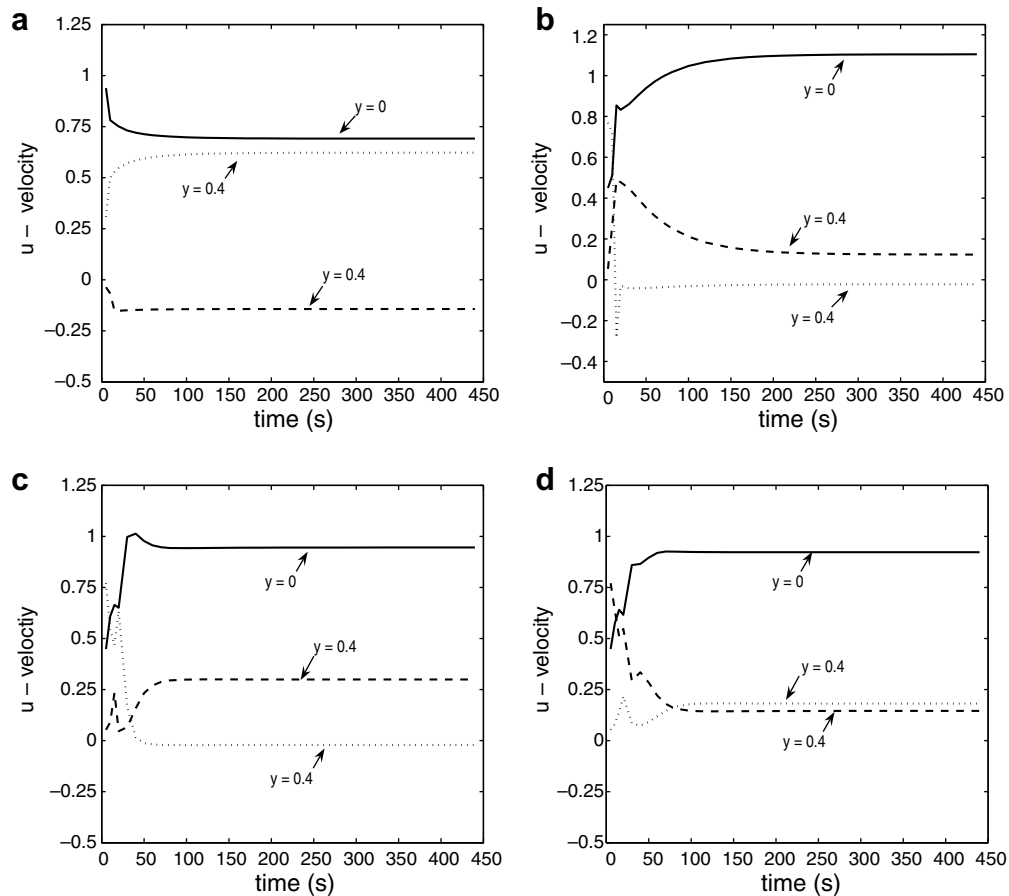


Fig. 14. Time histories of u -velocity component at different cross-sections: (a) $x = 3$; (b) $x = 6$; (c) $x = 9$; (d) $x = 12$.

values have been fixed with respect to inlet boundary values such a way that the boundary condition for ψ does not suffer from any discontinuity. At outlet, the condition $\frac{\partial \psi}{\partial x} = 0$ has been used in Eqs. (31)–(33) for ψ and ω .

4.5. Flow through vascular stenosis

The effect of axisymmetric constrictions in tubes has many important applications especially in biofluids. The partial occlusion of arteries due to stenotic obstruction is one of the most frequent anomalies in blood circulation. The results of a steady flow analysis for this situation is an important first step in studying the effects of arterial stenosis on the human body. It is well known that, once such obstruction is formed, the blood flow is significantly altered and fluid dynamic factors play an important role as the stenosis continues to develop. Studies of the stenotic flow fields have been done by numerous investigators. The fluid mechanical and biochemical effects associated with stenoses have been reported in many studies. One of the first numerical studies for flow through a constricted tube was done by Lee and Fung [34] with the use of a gaussian function to model the constriction. Later Young and Tsai [35] conducted a series of steady flow experiments with different levels of area constrictions and highlighted various hydrodynamic factors such as pressure drop, separation and turbulence. Deshpande et al. [36] have theoretically modelled vascular constrictions of a sinusoidal function and verified them with experimental results. Further, fluid flow through tubes with multiple constrictions has also been studied by Lee [37,38].

4.5.1. Geometry of the stenoses and governing equations

In the present study, models with single constriction (occlusion) have been considered. The tube has been assumed circular in cross-section with unit radius everywhere except at the location of the stenotic constriction. The governing equations of the three dimensional problem have been chosen in cylindrical polar co-ordinates to exploit the axisymmetric nature of the flow.

The cylindrical coordinate system (z, r, θ) having the z -axis coincident with the axis of the tube is assumed. The schematic of the flow is as given in Fig. 16. To describe the axisymmetric constriction centered at $z = 0$, both gaussian and cosine (the

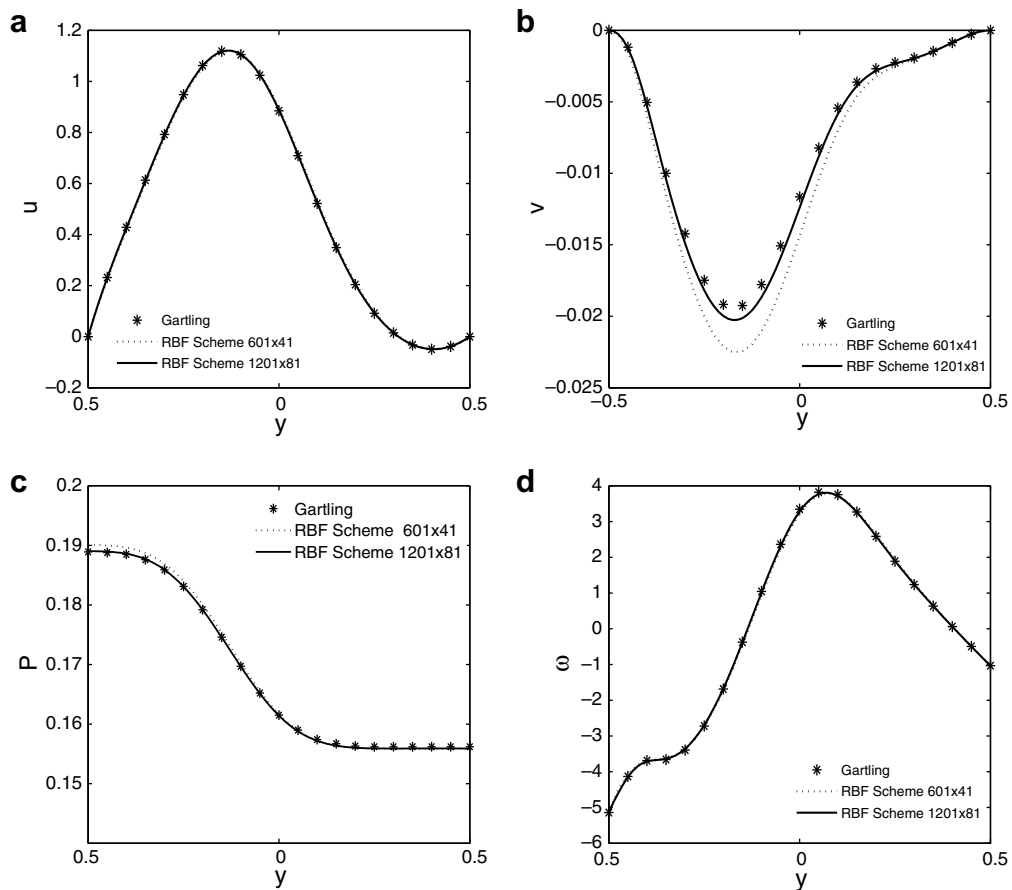


Fig. 15. Comparison of (a) u -velocity, (b) v -velocity, (c) Pressure and (d) vorticity at the cross-section $x = 7$ with [26].

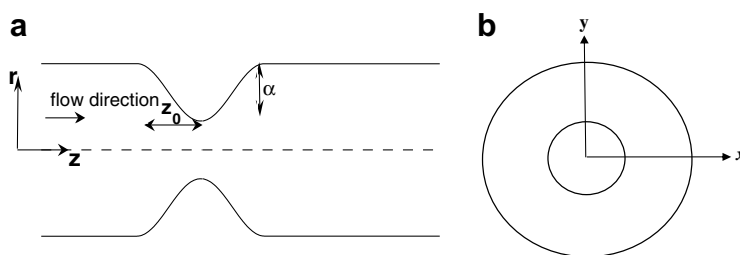


Fig. 16. (a) Side and (b) front view of stenoses geometry.

function used by Deshpande et al. [36]) functions have been considered. The results given in the following sections are based on the cosine function which can be defined as

$$r_0(z) = 1 - \frac{\alpha}{2} \left[1 + \cos \left(\frac{\pi z}{z_0} \right) \right], \quad -z_0 \leq z \leq z_0, \quad (36)$$

where z_0 defines the length and α defines the depth of the stenoses (Fig. 16a).

Since an axisymmetric solution is sought, all dependent variables are assumed to be independent of θ and also made the corresponding velocity component zero. Therefore, the governing equations for axisymmetric flow, in cylindrical polar coordinates, are given by

Continuity equation :

$$\frac{\partial u}{\partial z} + \frac{\partial v}{\partial r} + \frac{v}{r} = 0. \quad (37)$$

Momentum equations :

$$\frac{\partial u}{\partial t} + u \frac{\partial u}{\partial z} + v \frac{\partial u}{\partial r} = -\frac{\partial P}{\partial z} + \frac{1}{Re} \left[\frac{\partial^2 u}{\partial z^2} + \frac{\partial u^2}{\partial r^2} + \frac{1}{r} \frac{\partial u}{\partial r} \right], \quad (38)$$

$$\frac{\partial v}{\partial t} + u \frac{\partial v}{\partial z} + v \frac{\partial v}{\partial r} = -\frac{\partial P}{\partial r} + \frac{1}{Re} \left[\frac{\partial^2 v}{\partial z^2} + \frac{\partial v^2}{\partial r^2} + \frac{1}{r} \frac{\partial v}{\partial r} - \frac{v}{r^2} \right], \quad (39)$$

where (u, v) are the velocity components corresponds to physical co-ordinates (z, r) , P is the pressure and $Re = \frac{U_{\max} R}{\nu}$, where U_{\max} is maximum velocity and R is the radius of the pipe at the unoccluded region for the dimensional problem and ν is the kinematic viscosity. Eqs. (37)–(39) have been solved using the Algorithm 3.1 with the necessary minor changes.

The boundary conditions associated with the physical problem are defined as follows. At the wall $r = r_0(z)$, the usual no-slip boundary conditions have been taken. At the line of symmetry $r = 0$, a symmetry condition on u has been applied while v has been chosen as zero. These conditions can be defined as,

$$\frac{\partial u}{\partial r} = 0, \quad v = 0, \quad \text{at } r = 0. \quad (40)$$

Hagen-Poiseuille flow through a long circular tube of constant cross-section has been assumed at the inlet,

$$u = (1 - r^2), \quad v = 0, \quad \text{at } z = -\infty. \quad (41)$$

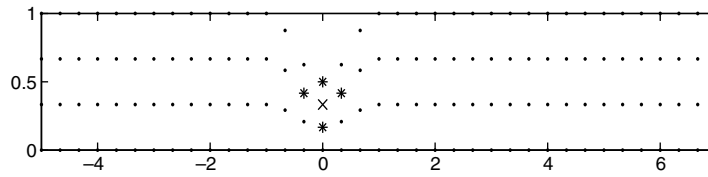


Fig. 17. Nodal distribution for stenoses problem.

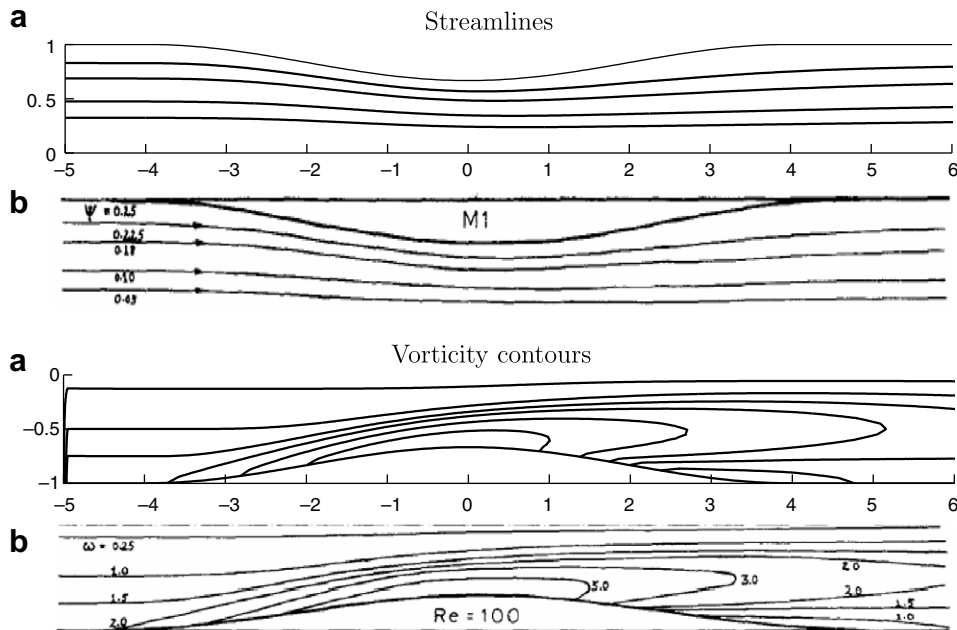


Fig. 18. Comparison of streamlines and vorticity contours for 56% area occlusion at $Re = 100$: (a) present; (b) [36].

Outflow boundary conditions, as mentioned in the case of flow over a backward-facing step, is a major concern even in stenoses problem. OBCs have to be formulated mathematically and in the present application, we have obtained the conditions by matching the governing equations at the outflow boundary.

Stenoses are commonly characterized as a percentage reduction in diameter or area of the tube. Due to the sudden reduction of the diameter at the constriction region of the tube the numerical schemes loose stability and tend to diverge. Therefore in the present study, two models have been considered with $\alpha = 0.333$ and $z_0 = 4$ and $\alpha = 0.5$ and $z_0 = 1$, that is with 56 and 75 percentages of area reductions, respectively. The computations are carried out for various Reynolds' numbers and steady state solutions have been obtained. The results have been compared with the results of Deshpande et al. [36], wherever they are available.

The distribution of the nodes considered for the computations has the structure as given in Fig. 17 (not all the nodes have been shown in the figure). A tensor-product type distribution is considered, which naturally made the distribution of the nodes in the stenoses region non-uniform. Due to this non-uniformity of nodal distribution, the 5-node support chosen in this region differ from the standard 5-node support and it is portrayed in Fig. 17. The domain chosen for the computations is $[-5, 25] \times [0, r_0(z)]$ with 301 nodes in z and 11 in r directions, respectively. Time step has been taken as 0.001 in all the computations. $\psi - \omega$ computations have been carried out by following the same procedure described for the previous test problems. Inlet boundary condition is obtained by integrating the u -velocity and then the same condition has been extended to outflow for ψ . Based on these values, rest of the boundary conditions have been fixed. The observations and comparisons are discussed in the following section.

4.5.2. 56% area occlusion

This is rather a mild constriction for which streamlines and vorticity contours have been compared in Fig. 18 with the available benchmark results at $Re = 100$. It can be seen that $Re = 100$ is rather very small to yield separated flow. Figs. 19 and 20 give the streamlines and vorticity contours at $Re = 400$ and 1600, respectively. These Reynolds' numbers are larger than the critical value such that the laminar separation takes place. As expected, the reattachment point tends asymptotically towards the far downstream as the Reynolds' number increased.

Simulations have been performed for Reynolds' numbers up to 1600 and the effect of stenosis has been examined using various parameters like velocities, pressure and vorticity, mainly on the symmetry line $r = 0$ and on the wall $r = r_0(z)$. Fig. 21a

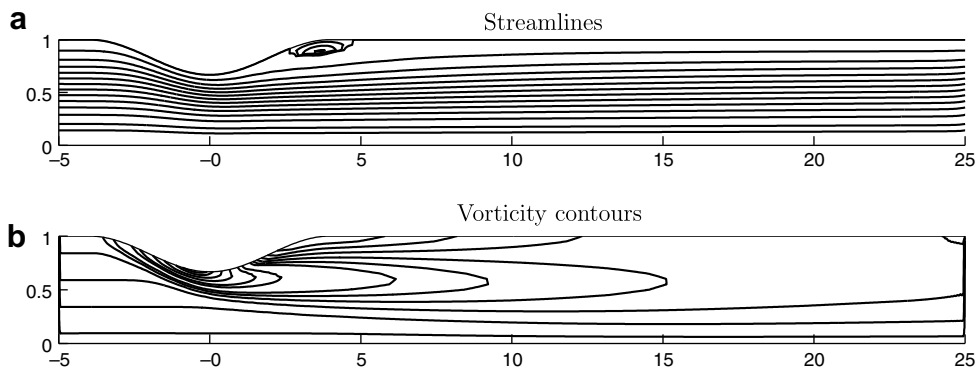


Fig. 19. Streamlines and vorticity contours for 56% area occlusion at $Re = 400$.

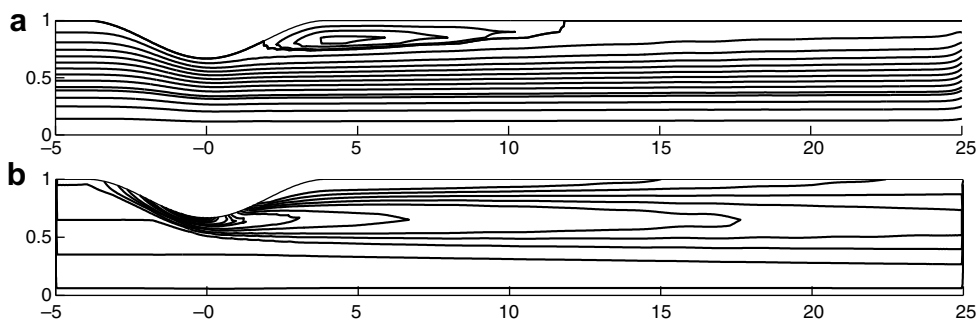


Fig. 20. Streamlines and vorticity contours for 56% area occlusion at $Re = 1600$.

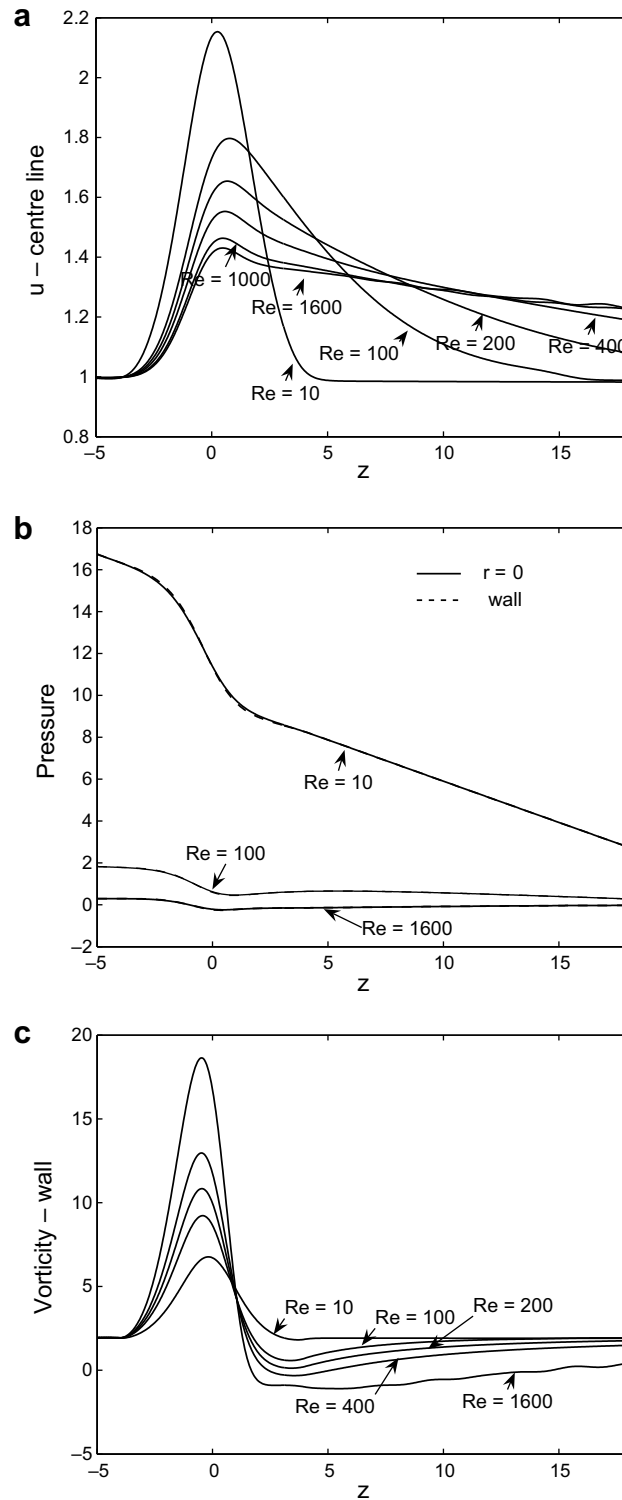


Fig. 21. (a) Axial velocity profile at the symmetry line $r=0$. (b) Pressure at the symmetry line $r=0$ and the wall. (c) Vorticity at the wall, at different Reynolds' numbers for 56% area occlusion.

illustrates the variation of pressure along the axis and on the wall. In the case of low Re , as the occlusion is approached, a rapid fall in the pressure can be observed. Vorticity at the wall for various Reynolds' numbers has been plotted in Fig.

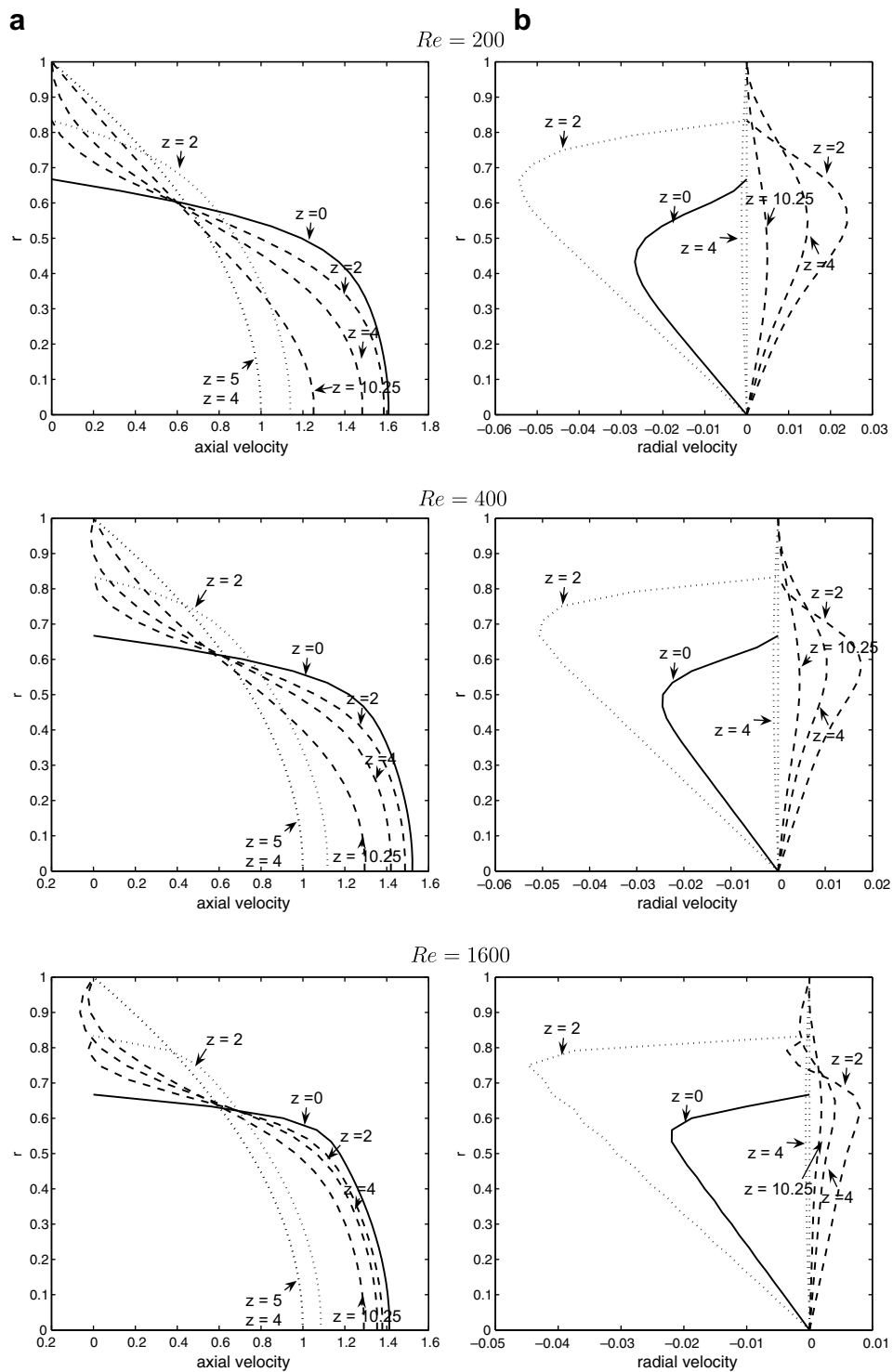


Fig. 22. (a) Axial and (b) radial velocities at different cross-sections of the stenosis for 56% area occlusion at Reynolds' numbers $Re = 200, 400$ and 1600 .

21b, where a large increase in the value is evident in the constriction with a maximum vorticity occur just before the centre of the occlusion. Also, for separated flows, change of sign in the vorticity can be observed near the end of the throat.

The variation of centre line velocity is illustrated in Fig. 21c. From this figure, it can be seen that the location of the maximum velocity for each Re is near the throat (on the downstream side) and these values slightly shift towards the down-

stream as Re increases. Also the decrease in the centre line velocity towards downstream is linear in z . The velocity fall after the occlusion is slow for large Reynolds' numbers, may be due to the low pressure variation (see Fig. 21a) in this region compared to small values of Re .

Fig. 22 gives profiles of both axial and radial velocities at various cross-sections at different values of Re . It can be seen that both the velocity components undergo change in sign within the recirculation region at the cross-sections chosen from the constricted region. At $Re = 200$, this does not happen since there is no separated flow.

4.5.3. 75% area occlusion

For 75% of area reduction, a relatively severe stenoses, separated flow occurs for relatively small Reynolds' numbers compared to the previous case. A very small separated region can be visualized in the streamline pattern given in Fig. 23 for $Re = 10$. Further, for $Re = 200$, the streamlines and iso-vorticity contours have been compared with that of Deshpande et al. [36] and given in Fig. 24. It can be seen that the reattachment point in this case is far below downstream compared to that of $Re = 10$.

From Fig. 25, it is clear that the trends are similar to that of 56% area occlusion, however, the peak values of vorticity and centerline velocity are far higher in 75% case. This is due to the larger expansion region in 75% case on account of high degree of area reduction.

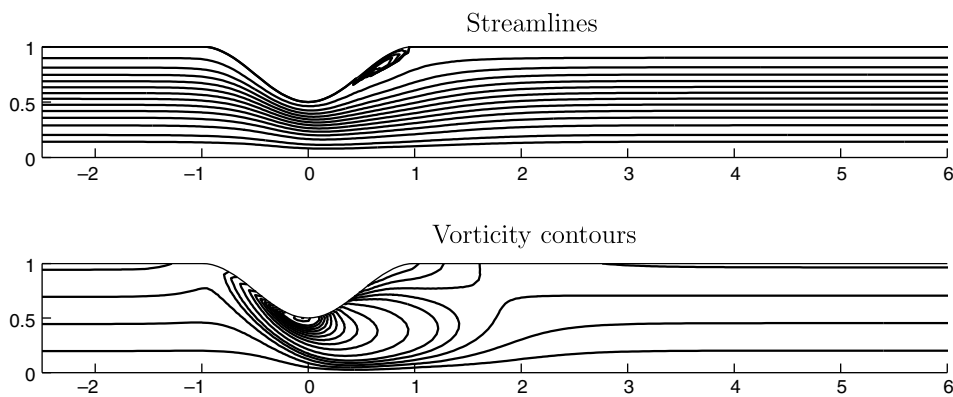


Fig. 23. Streamlines and vorticity contours for 75% area occlusion at $Re = 10$.

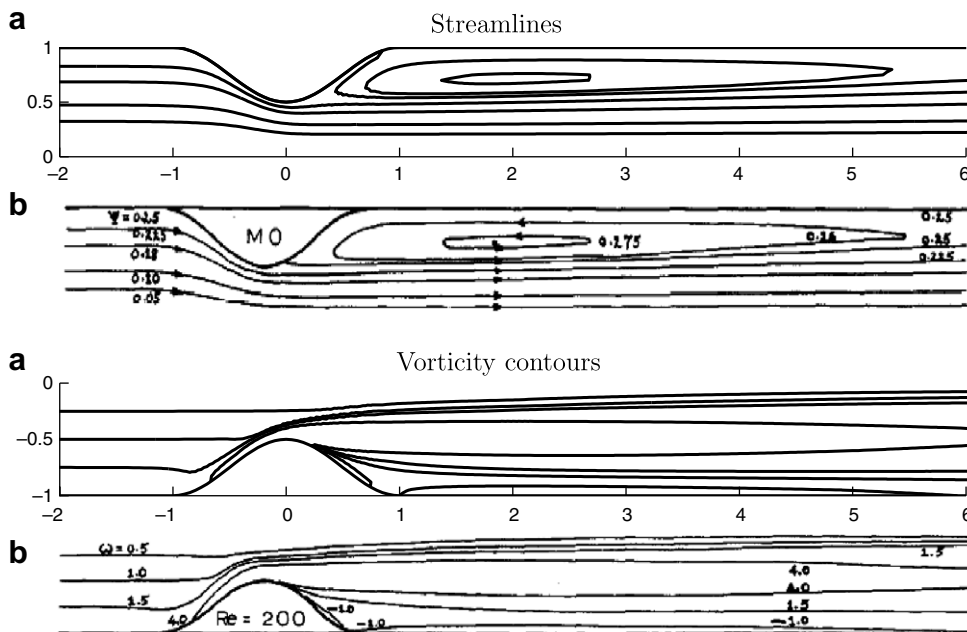


Fig. 24. Comparison of streamlines and vorticity contours for 75% area occlusion at $Re = 200$: (a) present; (b) [36].

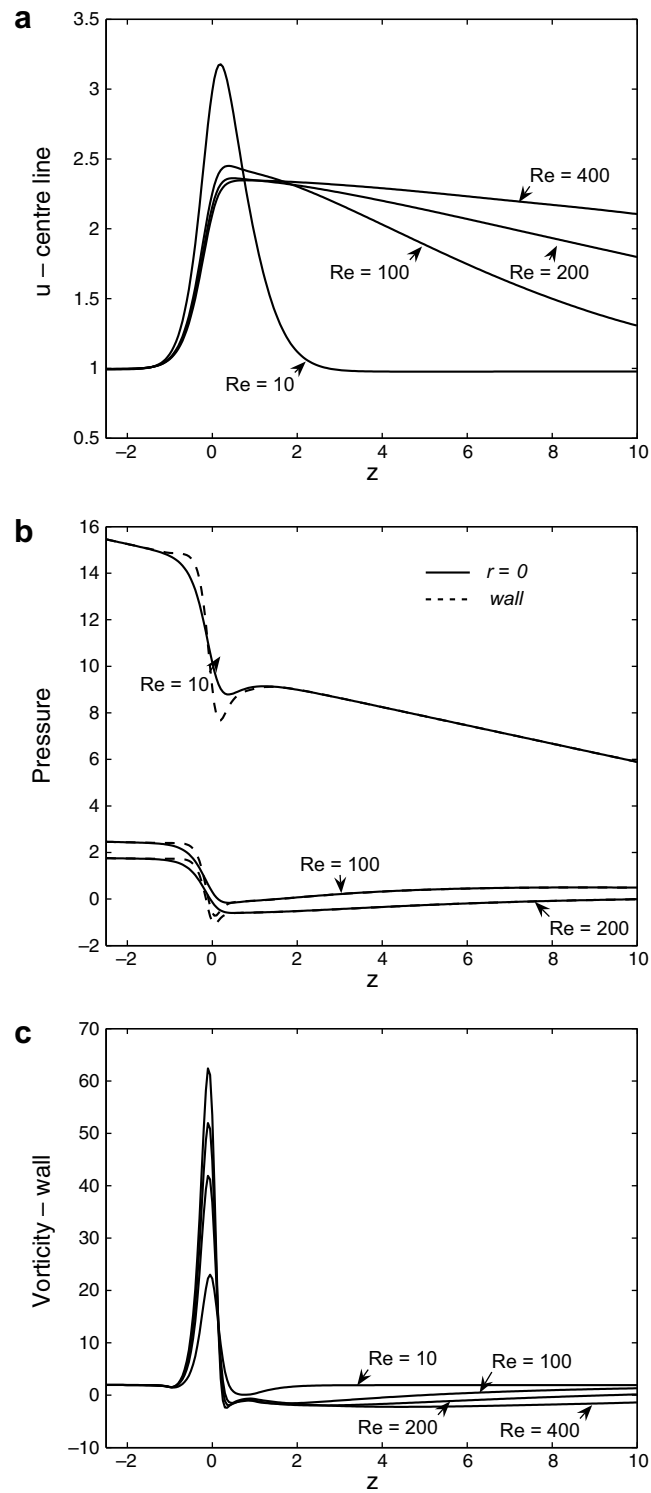


Fig. 25. (a) Axial velocity profile at the symmetry line $r=0$. (b) Pressure at the symmetry line $r=0$ and the wall. (c) Vorticity at the wall, at different Reynolds' numbers for 75% area occlusion.

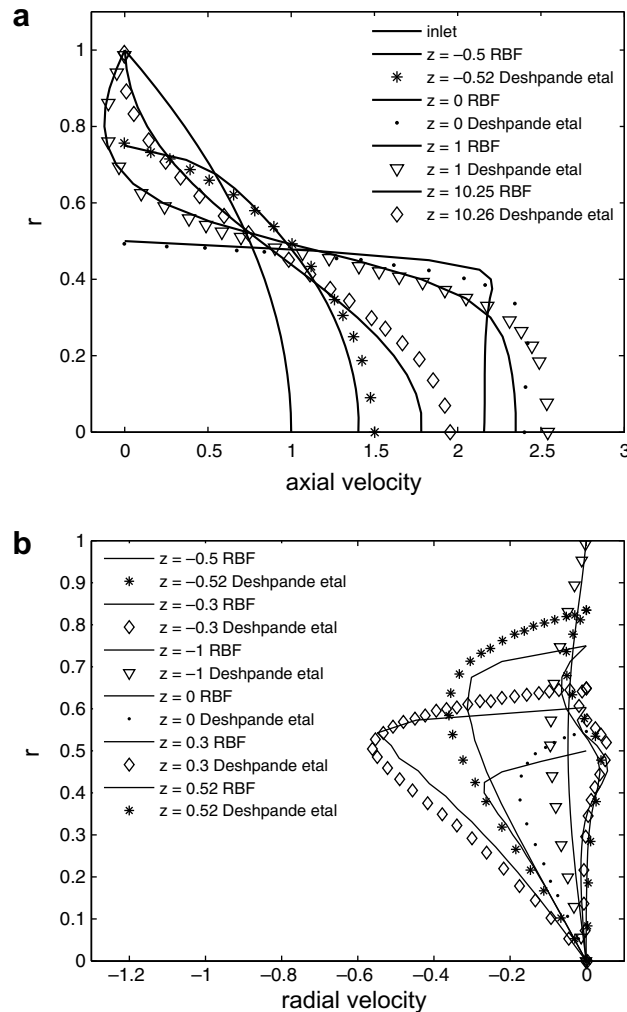


Fig. 26. Comparison of (a) axial and (b) radial velocities at various cross-sections of the stenosis with 75% occlusion for $Re = 200$.

In Fig. 26 axial and radial velocity components at $Re = 200$ have been compared with the results given by Deshpande et al. [36] and can be seen that the values agree reasonably well.

5. Conclusions

In the present investigation, a 'local' RBF gridfree scheme to solve unsteady, viscous, incompressible Navier–Stokes equations in primitive variables has been developed. A novel fractional step algorithm has been proposed to achieve velocity–pressure decoupling. The developed scheme has been validated over various problems. Simple problems like Couette flow or Poiseuille flow gave very accurate solutions even with coarser distribution of the nodes. The shape parameter in the multiquadric and different support domains have been experimented on these problems and the results have been used to fix the shape parameter and the support domain for the rest of the problems. Complex features in lid driven cavity flow have been accurately predicted with the present scheme, especially using appropriate non-uniform nodal distribution, even for large Reynolds' numbers.

Further, the study of the developed scheme has been extended to problems with separated flows, i.e. flow over a BFS and flow through vascular stenoses, and the results obtained have been in excellent agreement with the available benchmark solutions. For BFS flow, steady state solutions have been obtained for $Re = 800$ even with coarser distribution of the nodes, unlike the claim made by Kaiktsis et al. [23]. For stenotic flows, both mild (56%) and severe (75%) area reductions have been analysed by considering streamline patterns, vorticity, pressure and velocity. Some of the results have been compared with that of the available results given by Deshpande et al. [36] and found them satisfactory.

References

- [1] E.J. Kansa, Multiquadrics – a scattered data approximation scheme with applications to computational fluid dynamics – II solutions to parabolic, hyperbolic and elliptic partial differential equations, *Comput. Math. Appl.* 19 (1990) 147–161.
- [2] G.E. Fasshauer, Solving partial differential equations by collocation with radial basis functions, in: A. Le Méhauté, C. Rabut, L.L. Schumaker (Eds.), *Surface Fitting and Multiresolution Methods*, Vanderbilt University Press, 1997, pp. 131–138.
- [3] Z. Wu, Hermite–Birkhoff interpolation of scattered data by radial basis functions, *Approx. Theory Appl.* 8 (2) (1992) 1–10.
- [4] Y.C. Hon, R. Schaback, On unsymmetric collocation by radial basis functions, *Appl. Math. Comput.* 119 (2–3) (2001) 177–186.
- [5] B. Šarler, A radial basis function collocation approach in computational fluid dynamics, *CMES Comput. Model. Eng. Sci.* 7 (2) (2005) 185–193.
- [6] S. Chantasiriwan, Performance of multiquadric collocation method in solving Lid-driven cavity flow problem with low Reynolds number, *CMES Comput. Model. Eng. Sci.* 15 (2006) 137–146.
- [7] N. Mai-Duy, T. Tran-Cong, An efficient indirect RBFN-based method for numerical solution of PDEs, *Numer. Methods Partial Differ. Eq.* 21 (4) (2005) 770–790.
- [8] N. Mai-Duy, L. Mai-Cao, T. Tran-Cong, Computation of transient viscous flows using indirect radial basis function networks, *CMES Comput. Model. Eng. Sci.* 18 (1) (2007) 59–77.
- [9] W. Chen, Y.C. Hon, Numerical convergence of boundary knot method in the analysis of Helmholtz, modified Helmholtz and convection–diffusion problems, *Comput. Methods Appl. Mech. Eng.* 192 (2003) 1859–1875.
- [10] W. Chen, M. Tanaka, A meshless, integration-free, and boundary-only RBF technique, *Comput. Math. Appl.* 43 (2002) 379–391.
- [11] C.S. Chen, C.A. Brebbia, H. Power, Dual reciprocity method for Helmholtz-type operators, *Bound. Elem.* 20 (1998) 495–504.
- [12] G.B. Wright, B. Fornberg, Scattered node compact finite difference-type formulas generated from radial basis functions, *J. Comput. Phys.* 212 (2006) 99–123.
- [13] C.K. Lee, X. Liu, S.C. Fan, Local multiquadric approximation for solving boundary value problems, *Comput. Mech.* 30 (2003) 396–409.
- [14] A.I. Tolstykh, D.A. Shirobokov, On using radial basis functions in a “finite difference mode” with applications to elasticity problems, *Comput. Mech.* 33 (2003) 68–79.
- [15] B. Šarler, R. Vertnik, Meshfree explicit local radial basis function collocation method for diffusion problems, *Comput. Math. Appl.* 51 (2006) 1269–1282.
- [16] R. Vertnik, B. Šarler, Meshless local radial basis function collocation method for convective–diffusive solid–liquid phase change problems, *Int. J. Numer. Methods Heat Fluid Flow* 16 (5) (2006) 617–640.
- [17] F. Harlow, J. Welch, Numerical calculation of time dependent viscous flow of fluid with free surface, *Phys. Fluids* 8 (1965) 212–218.
- [18] A.J. Chorin, A numerical method for solving incompressible viscous flow problems, *J. Comput. Phys.* 2 (1967) 12–26.
- [19] J. Kim, P. Moin, Application of a fractional-step method to incompressible Navier–Stokes equations, *J. Comput. Phys.* 59 (1985) 308–323.
- [20] R.L. Hardy, Multiquadric equations of topography and other irregular surfaces, *J. Geophys. Res.* 76 (1971) 1905–1915.
- [21] R. Franke, Scattered data interpolation: test of some methods, *Math. Comput.* 48 (1982) 181–200.
- [22] U. Ghia, K.N. Ghia, C.T. Shin, High-Re solutions for incompressible flow using the Navier–Stokes equations and a multigrid method, *J. Comput. Phys.* 48 (1982) 387–411.
- [23] L. Kaiktsis, G.E. Karniadakis, S.A. Orszag, Onset of three-dimensionality, equilibria, and early transition in flow over a backward-facing step, *J. Fluid Mech.* 231 (1991) 501–528.
- [24] A.W. Runchal, Benchmark problems for heat transfer codes, in: B. Blackwell, D.W. Pepper (Eds.), *Proceedings of Winter Annual Meeting ASME*, Anaheim, CA, 1992, pp. 13–20.
- [25] D. Choudhury, Benchmark problems for heat transfer codes, in: B. Blackwell, D.W. Pepper (Eds.), *Proceedings of Winter Annual Meeting ASME*, Anaheim, CA, 1992, pp. 53–59.
- [26] D.A. Gartling, A test problem for outflow boundary conditions – flow over a backward-facing step, *Int. J. Numer. Methods Fluids* 11 (1990) 953–967.
- [27] P.M. Gresho, D.K. Gartling, J.R. Torczynski, K.A. Cliffe, K.H. Winters, T.J. Garratt, A. Spence, J.W. Goodrich, Is the steady viscous incompressible two-dimensional flow over a backward-facing step at $Re = 800$ stable?, *Int. J. Numer. Methods Fluids* 17 (1993) 501–541.
- [28] J. Keskär, D.A. Lyn, Computations of a laminar backward-facing step flow at $Re = 800$ with a spectral domain decomposition method, *Int. J. Numer. Methods Fluids* 29 (1999) 411–427.
- [29] G. Comini, M. Manzan, C. Nonino, Finite element solution of the streamfunction–vorticity equations for incompressible two-dimensional flows, *Int. J. Numer. Methods Fluids* 19 (1994) 513–525.
- [30] T.W.H. Sheu, S.F. Tsai, Consistent Petrov–Galerkin finite element simulation of channel flows, *Int. J. Numer. Methods Fluids* 31 (1999) 1297–1310.
- [31] R.L. Sani, P.M. Gresho, Resume and remarks on the open boundary condition minisymposium, *Int. J. Numer. Methods Fluids* 18 (1994) 983–1008.
- [32] M.A. Cruchaga, A study of the backward-facing step problem using a generalized streamline formulation, *Commun. Numer. Methods Eng.* 14 (1998) 697–708.
- [33] M. Ramsak, L. Skerget, A subdomain boundary element method for high-Reynolds laminar flow using stream function–vorticity formulation, *Int. J. Numer. Methods Fluids* 46 (2004) 815–847.
- [34] J.S. Lee, Y.C. Fung, Flow in locally constricted tubes at low Reynolds numbers, *J. Appl. Mech.* 37 (1970).
- [35] D.F. Young, F.Y. Tsai, Flow characteristics in models of arterial stenosis – I. Steady flow, *J. Biomech.* 6 (1973) 395–410.
- [36] M.D. Deshpande, D.P. Giddens, R.F. Mabon, Steady laminar flow through modelled vascular stenosis, *J. Biomech.* 9 (1976) 165–174.
- [37] T.S. Lee, Numerical studies of fluid flow through tubes with double constrictions, *Int. J. Numer. Methods Fluids* 11 (1990) 1113–1126.
- [38] T.S. Lee, A false transient approach to steady state solution of fluid flow through vascular constrictions, *Comput. Mech.* 7 (1991) 269–277.